

Role of silicon and carbon on the structural and electrochemical properties of Si-Ni_{3,4}Sn₄-Al-C anodes for Li-ion batteries

Tahar Azib^{a*+}, Claire Thaury^{a,b*}, Cécile Fariaut-Georges^a, Thierry Hézèque^b, Fermin Cuevas^a, Christian Jordy^b and Michel Latroche^a

^aUniv. Paris Est Creteil, CNRS, ICMPE, UMR7182, F-94320, Thiais, France.

^bSAFT Batteries, 113 Bd. Alfred Daney, 33074 Bordeaux, France.

Abstract

Varying the amounts of silicon and carbon, different composites have been prepared by ball milling of Si, Ni_{3,4}Sn₄, Al and C. Silicon and carbon contents are varied from 10 to 30 wt.% Si, and 0 to 20 wt.% C. The microstructural and electrochemical properties of the composites have been investigated by X-Ray Diffraction (XRD), Scanning Electron Microscopy (SEM) and electrochemical galvanostatic cycling up to 1000 cycles. Impact of silicon and carbon contents on the phase occurrence, electrochemical capacity and cycle-life are compared and discussed. For C-content comprised between 9 and 13 wt.% and Si-content ≥ 20 wt.%, Si nanoparticles are embedded in a Ni_{3,4}Sn₄-Al-C matrix which is chemically homogeneous at the micrometric scale. For other carbon contents and low Si-amount (10 wt.%), no homogeneous matrix is formed around Si nanoparticles. When homogenous matrix is formed, both Ni₃Sn₄ and Si participate to the reversible lithiation mechanism, whereas no reaction between Ni₃Sn₄ and Li is observed for no homogenous matrix. Moreover, best cycle-life performances are obtained when Si nanoparticles are embedded in a homogenous matrix. Composites with carbon in the 9-13 wt.% range and 20 wt.% silicon lead to the best balance between capacity and life duration upon cycling. This work experimentally demonstrates that embedding Si in an intermetallic/carbon matrix allows to efficiently accommodate Si volume changes on cycling

to ensure long cycle-life.

Keywords: Li-ion batteries, anodes, mechanical milling, intermetallic compounds, silicon

*Both authors contributed equally to this manuscript

+ Corresponding author

• E-mail address: azib@icmpe.cnrs.fr

• Full postal address: CNRS, ICMPE, UMR7182, 2 rue Henri Dunant, F-94320, Thiais, France

1. Introduction

Energy storage demands for current and future portable electronic devices and electrical vehicles are ever growing. Performances of Li-ion batteries in terms of specific power and density surpass other rechargeable battery systems but are still unsatisfactory for many applications such as extended-range electric vehicles [1–3]. The development of advanced anode materials exhibiting higher capacity than current graphite electrodes ($C = 370 \text{ mAhg}^{-1}$) remains very challenging [4]. Presently a lot of materials are studied as alternatives for carbonaceous ones to enhance the energy density of the negative electrode using various strategies such as conversion or alloying reactions [5,6]. For the latter, a special interest is brought to *p*-bloc elements that form lithiated compounds [7]. For instance Sn and Si can form $\text{Li}_{4.4}\text{Sn}$ and $\text{Li}_{3.75}\text{Si}$ compounds to store respectively 994 and 3600 mAhg^{-1} in electrochemical units, leading to much higher capacities than that of graphite [8,9]. In addition to their high theoretical capacity, these elements exhibit low potential and environmental friendliness, both suitable as anode properties.

However, electrodes made of pure *p*-bloc elements are considered inappropriate because of large capacity fading during electrochemical cycling [10]. The large volume expansion that accompanies Li insertion and extraction during cycle life results in electrode pulverization and loss of electrical contact [11,12]. To ensure mechanical stability, embedding capacitive elements into a buffering matrix that helps accommodating volume changes, while improving electronic conduction, has been proposed [13,14]. This concept can be implemented, for instance, using binary intermetallic compounds made of one element that reacts with lithium (*e.g.* Si or Sn) and another one that is inactive (*e.g.* Fe, Ni, Co or Cu). Some reported intermetallics to achieve this goal are Ni_3Sn_4 [15–17], Cu_6Sn_5 [18], CoSn_2 [19,20], FeSn_2 [20],

FeSi₂ [21] and NiSi₂ [22]. This approach has been successfully extended to ternary silicides such as Ti₄Ni₄Si₇ [23,24], TiFeSi₂ [25] and Ti₃Si₂C₂ [26]. Moreover, binary and ternary intermetallics have been associated to carbonaceous materials to form highly efficient multi-component systems, such as Si/FeSi₂/C [27] and Si/Cu₃Si/C [28], for further improvement of both the mechanical cohesion of silicon and the electronic conductivity of the whole active material.

In this context, an efficient composite Si-Ni_{3,4}Sn₄-Al-C has been already synthesized by mechanochemistry [29]. It consists of sub-micrometric Si particles embedded in a nanostructured and complex matrix mainly formed by Ni_{3,4}Sn₄ intermetallic compound and disordered carbon. Si and Sn are the capacitive elements whereas Ni and C are expected to accommodate the volume changes and to insure good electronic as well as ionic conductivity of the electrode material. Al addition is based on reported beneficial effects on the cycle-life of Si-Sn-Al amorphous electrodes [30], best results being obtained for the composition 30Si-67Sn-3Al which contains 3 wt.% of Al. This composite exhibits high reversible capacity (~700 mAhg⁻¹) and long cycle life (over 280 cycles) [31,32]. Here we investigate the influence of silicon and carbon contents on the microstructure of this composite material and its electrochemical properties. Silicon and carbon contents were varied from 10 to 30 wt.% Si, and from 0 to 20 wt.% C, respectively.

2. Experimental

Seven nanostructured composites Si-Ni_{3,4}Sn₄-Al-C with various carbon and silicon contents have been synthesized. Their overall compositions (weight percent) are given in Table 1. Two series were considered: i) for constant Si-content (~20 wt.%), the carbon amount was increased from 0 to 20 wt.% and ii) for constant C-content (13 wt.%), the silicon content was increased from 10 to 30 wt.%. Variation of C and Si contents were counterbalanced by the amount of

Ni_{3.4}Sn₄ intermetallic compound.

The composites were made in two steps. Firstly, a tin-based intermetallic precursor Ni_{3.4}Sn₄ was synthesized by powder metallurgy followed by mechanical milling of this intermetallic with Si, Al and C elements. To synthesize Ni_{3.4}Sn₄, elemental nickel (99.9 %, <45 μm, Cerac) and tin (99.9 %, <45 μm, Alfa-Aesar) powders were mixed in 3.4:4 atomic ratio, pelleted and sintered under argon atmosphere in a silica tube at 700°C for 7 days. This annealing time was necessary to obtain single-phase compound. The pellets were mechanically pulverized down to 125 μm size. Then, powders of silicon (99.9 %, <1 μm), aluminum (99 %, ≤ 75 μm, Aldrich), graphite and Ni_{3.4}Sn₄ were weighted according to the different compositions given in Table 1 and mechanically milled in a Fritsch Pulverisette 7 planetary mill. Ball milling was performed under argon atmosphere for 20 hours in an 80 ml volume jar with 7 mm diameter balls. The ball-to-powder weight ratio was 5:1. Both jar and balls are made of stainless steel. Vial rotation speed of the mill was 600 rpm.

The crystal structure of the milled composites was analyzed by XRD with a Bruker D8 advance θ - θ diffractometer using Cu K α radiation. Diffraction patterns were analyzed by the Rietveld method using the FullProf software [33]. Phase assignation and refinement of their crystal structure including lattice parameters, phase amounts, peak-profile factors were undertaken. Crystal sizes were evaluated from the Lorentzian contribution to the Thompson–Cox–Hastings pseudo–Voigt profile-shape function used in the Rietveld analysis, after considering the instrumental contribution [34]. For Ni_{3.4}Sn₄, variations of the Ni overstoichiometry were obtained from the refinement of partial occupancy of Ni at site 2c (0, 0, ½) in C2/m space group [35]. The microstructure of 20h-milled composites (*i.e.* phase distribution and morphology) was studied by scanning electron microscopy (SEM) using a SEM-FEG MERLIN ZEISS device. The SEM images were collected in Back-Scattered Electron (BSE) mode at cross-sections of the ball-milled composite powders. The composites were embedded

in epoxy resin then polished and metalized with platinum. Point-by-point composition analysis was carried out by Energy-Dispersive-X-ray (EDX) analysis.

Electrochemical measurements were carried out by galvanostatic cycling in coin-type half-cells. Working electrode material was prepared by mixing 55 wt.% of the composite sieved under 125 μm , 20 wt.% of carboxymethyl-cellulose (CMC) binder and 25 wt.% of carbon black. Low loading of the composite material (55 wt.%) was selected to avoid limitations on its intrinsic electrochemical properties due to electrode formulation. Metallic lithium was used as counter negative electrode. The electrolyte consisted of 1 M solution of LiPF_6 dissolved in ethylene carbonate (EC)/propylene carbonate (PC)/dimethyl carbonate (DMC) (1:1:3 vol./vol./vol.). A polyolefin Celgard® microporous membrane and a nonwoven polyolefin membrane were used as separators. The battery was assembled in an argon-filled glove box. The experiments were performed using a Biologic VMP3 potentiostat at a typical cycling-rate of C/10 (full capacity C in 10 hours) with potential window comprised between 70 mV and 2 V. Different conditions were used for the first three cycles and every 20 cycles. To fully activate Si particles, the first cycle was performed at slow rate C/50 with a cut-off voltage of 0 V. The second cycle was performed at medium rate C/20 with a cut-off voltage of 10 mV. This cycle aimed to get to obtain the maximal capacity avoiding lithium deposition on the active material. The third cycle was also done at C/20 but with higher cut-off potential (70 mV) to improve cycle-life. Cycles performed following the latter protocol are named hereafter reference cycles. They were done on the third and every twenty cycles. Otherwise specified, only reference cycles are reported in this paper.

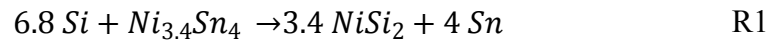
3. Results

3.1. Structural and microstructural characterization

All composites have been characterized by X-ray diffraction and Table 2 gathers the

structural and microstructural data obtained from the Rietveld analysis. Graphical output of the Rietveld analysis for each composite with their corresponding Rietveld agreement factors are gathered in Fig. S1 (Supplementary Information).

A carbon-free composite was first synthesized with the nominal composition $\text{Si}_{0.22}\text{Ni}_{0.22}\text{Sn}_{0.53}\text{Al}_{0.03}$. XRD patterns of this sample before and after 20-hour milling are displayed in Fig. 1. The observed diffraction lines can be attributed to different phases shown at the bottom of the figure. Before milling, main peaks are indexed with diffraction lines belonging to Si (S.G. = $Fd\bar{3}m$, $a = 5.430 \text{ \AA}$) and $\text{Ni}_{3,4}\text{Sn}_4$ (S.G. = $C2/m$, $a = 12.37 \text{ \AA}$, $b = 4.069 \text{ \AA}$ and $\beta = 104.06$) [36]. After milling, besides minor contribution of initial reactants Si and $\text{Ni}_{3,4}\text{Sn}_4$, main diffraction peaks in the XRD pattern can be indexed with two novel phases: NiSi_2 (S.G. = $Fm\bar{3}m$, $a = 5.406 \text{ \AA}$) and $\beta\text{-Sn}$ (S.G. = $I4_1/amd$, $a = 5.832 \text{ \AA}$, $a = 3.182 \text{ \AA}$) [36]. The formation of both phases is attributed to the mechanochemically induced reaction R_1 between the intermetallic and the silicon as follows:



As the diffraction peaks of Si and NiSi_2 strongly overlap, it is hard to detect NiSi_2 formation by XRD. The occurrence of $\beta\text{-Sn}$ is easier to be detected by XRD due to its high scattering power, though main diffraction peaks of $\beta\text{-Sn}$ partially overlap with those of $\text{Ni}_{3,4}\text{Sn}_4$. Thus, $\beta\text{-Sn}$ diffraction peaks can serve as markers of reaction R_1 [31]. Note that no diffraction peaks related to Al have been detected. The low Al content used (3 wt.%), Al amorphization or dissolution into other detected phases may explain this result. This is a common feature of all composites synthesized in this research and will not be further discussed.

Fig. 2 shows the XRD patterns of the composites ranging from 9 to 20 wt.% of carbon for constant Si content (20 wt.% Si). After 20 hours of milling, diffraction lines from $\text{Ni}_{3,4}\text{Sn}_4$, $\beta\text{-Sn}$ -phase and Si/ NiSi_2 are identified. Changes with C-content in the relative intensity of

diffraction peaks at $2\theta \sim 44$ indicate minor occurrence of reaction R_1 , especially for low C-content. Indeed, Rietveld analysis results (Table 2) show that on increasing the C-content from 0 to 20 wt.%, the Sn and NiSi_2 amounts decrease from 42 to 0.7 wt.% and from 28 wt.% to no detection, respectively. This reveals that the presence of carbon significantly reduces the extent of reaction R_1 .

Significant peak broadening of intermetallic $\text{Ni}_{3.4}\text{Sn}_4$ is also observed after milling. It is attributed to crystallite size reduction and this phenomenon is more significant for the lower carbon contents. The crystallite size L of $\text{Ni}_{3.4}\text{Sn}_4$ varies from 8 to 50 nm when C-content increases from 0 to 20 wt.%. In addition, the Ni over-stoichiometry x of the intermetallic phase decreases from 0.6 to 0.1 on reducing the C-content (Table 2), which concurs with the homogeneity domain of $\text{Ni}_{3+x}\text{Sn}_4$ [35]. These results evidence that the crystallographic properties of the intermetallic phase are strongly dependent on the use of carbon as process control agent (PCA) during milling. When the C-content decreases, the crystallite size of the intermetallic phase diminishes, and Ni atoms partially segregate out of $\text{Ni}_{3.4}\text{Sn}_4$.

Fig. 3 shows the XRD patterns of the composites ranging from 10 to 30 wt.% of silicon (*i.e.* at a constant 13 wt.% C-content). Whatever the Si content, peak broadening is very similar for the three compositions and Rietveld analyses lead to comparable crystallite sizes. After milling, diffraction lines from $\text{Ni}_{3.4}\text{Sn}_4$ and Si are still clearly identified. Nonetheless, as for the carbon series, changes in the Sn content related to reaction R_1 are observed. The Sn amount gradually increases from 0.5 wt.% to 6 wt.% when Si content increases from 10 to 30 wt.%.

Fig. 4 shows the cross-section SEM-BSE micrographs of the carbon-containing composites milled for 20 hours. At constant Si-amount (20 wt.%), from top to bottom of Fig. 4, the microstructure of low-content carbon composites (9 and 13 wt.%) consist of spherical dark areas, ~ 100 nm in size, surrounded by a grey matrix. In contrast, the richer carbon composites (17 and 20 wt%) show a mixture of dark, grey and micrometric bright areas of

variable size. EDX analysis has been done for the 9 wt.% carbon-containing composite to identify the phases related to the different contrasts (Fig. 5). Dark and bright areas correspond to silicon and $\text{Ni}_{3,4}\text{Sn}_4$, respectively, whereas grey parts contain all elements: silicon, nickel, tin, aluminum and carbon, which are intimately mixed at the spatial resolution of EDX point-analysis (< 100 nm). Therefore, for low carbon contents (9 and 13 wt.%) Si nanoparticles are embedded in a homogenous and multi-elementary matrix, whereas at high carbon contents (17 and 20 wt.%) a heterogeneous mixture of Si nanoparticles, micrometric $\text{Ni}_{3,4}\text{Sn}_4$ and C-containing areas is observed.

At constant C-amount (13 wt.%), from left to right of Fig. 4, the 10 wt.% silicon composite consists in silicon (dark) nanoparticles surrounded by heterogeneous mixture of micrometric $\text{Ni}_{3,4}\text{Sn}_4$ (bright) and carbon-containing areas. For 20 and 30% of silicon, the microstructure of the composites is very similar to that of the lowest carbon content (9 wt.%) with silicon particles (dark) embedded in a homogeneous and multi-elementary matrix (grey).

As it will be later shown, the formation of the multi-elementary and homogenous matrix around Si nanoparticles is a key issue for the cycling stability of the composite. It should be noted that, based on XRD analysis (Fig. 2 and Fig. 3), Ni and Sn elements in this matrix are associated in the form of nanostructured $\text{Ni}_{3,4}\text{Sn}_4$ phase.

3.2. Electrochemical properties

The capacity retention on galvanostatic cycling has been initially analyzed for the five composites at constant Si-amount (20 wt.%) and increasing carbon content from 0 to 20 wt.%. Table 3 gathers relevant electrochemical properties in terms of reversible and irreversible capacities as well as capacity fading on cycling compared to the $C_{\text{upper limit}}$. This upper limit is determined from the overall composite composition (Table 1) and assuming that all active elements can fully react with lithium according to their individual electrochemical capacities:

3600, 994, 990 and 370 mAhg⁻¹ for Si, Sn, Al and C, respectively [7]. For the carbon-free composite, the evolution of reversible capacity on cycling for reference cycles is shown in Fig. S2 (Supplementary Information). Though it provides high discharge capacity in the first cycle, $C_{\text{lith,1st}} = 949 \text{ mAhg}^{-1}$, this composite suffers from severe capacity-loss on cycling with a final capacity of $C_{\text{lith,206th}} = 210 \text{ mAhg}^{-1}$. For 9 to 17 wt.% C composites, almost 100% of upper-limit capacity is recovered in the first lithiation (95, 98 and 97% for 9, 13 and 17wt.% C composites, respectively). Interestingly, all these 3 composites have low irreversibility, less than 18% in the first cycle. For C-containing composites, the evolution of reversible capacity upon cycling is displayed in Fig. 6. All composites have slightly lower capacities than the upper limit and high reversible capacities around 700 mAhg⁻¹ at the third cycle, except for the highest carbon content, 20 wt.%, that drops to 520 mAhg⁻¹ (Table 3). As concerns capacity fading upon cycling, it increases regularly from 0.024 up to 0.073 %/cycle with carbon content. Finally, coulombic efficiencies have been determined (Fig. S3, Supplementary Information). They are close to 100% without clear differences with the composition.

Fig. 7a shows the potential profiles of the first galvanostatic cycle for the 9 and 20 wt.%-carbon composites. For the first discharge, upon lithiation, capacities of 1196 and 923 mAhg⁻¹ are achieved for 9 and 20 wt.% of carbon, respectively. Upon charging, capacities of 985 and 702 mAhg⁻¹ are obtained. Two different potential features can be noticed in the discharging profiles. For the 9 wt.%-C composite, a sharp potential drop between E_{ini} 1.5 V and 0.5 V is first observed. Then, a large pseudo-plateau starting from 0.5 V down to the end of discharge (0 V) occurs. This plateau is attributed to the gradual formation of Li-Sn and Li-Si alloys by lithiation of Ni_{3,4}Sn₄ and Si, respectively. In contrast, for the 20 wt.%-C composite, the potential decrease quickly from 1.5 V to 0.15 V, followed by a shorter sloping plateau down to 0 V. The polarization is larger in the richest carbon composite. The irreversible capacities attributed to the formation of the SEI layer at the first cycle are 18 and 24% for 9 and 20 wt.% C

composites, respectively.

Fig. 7b shows the dependence of differential capacity (dQ/dV) vs potential for the two-representative carbon-containing composites (9 and 20 wt.%) at the third cycle. For the carbon-rich one (20 wt.%), two main peaks are observed both during lithiation and delithiation. The lithiation peaks at 0.24 and 0.09 V are characteristic of the alloying reaction of lithium with amorphous silicon to form Li_ySi amorphous phases. Amorphous silicon is widely reported to be formed during the first cycle [37,38]. Jimenez *et al.* [39] reported that the reduction peak at 0.24 V is associated with the formation of LiSi from the amorphous Si and subsequent phase transition from LiSi to Li_7Si_3 . The second reduction peak at 0.09 V is attributed to the formation of $\text{Li}_{13}\text{Si}_4$ phase. For the delithiation sweep, two distinct peaks appear at 0.28 V and 0.49 V. They are attributed to the full decomposition of Li_ySi phases into silicon [40,41]. It should be noted that no evidence of lithiation/delithiation peaks due to the reaction between $\text{Ni}_{3,4}\text{Sn}_4$ and lithium are detected for the 20 wt.%-C composite. For the carbon poor composite (9 wt.%-C), broad lithiation/delithiation peaks are observed for Si at 0.18/0.46 V and 0.09/0.28 V for reduction/oxidation reactions, respectively. In addition, extra peaks at 0.3 V for lithiation and 0.57 V for delithiation are observed. This redox pair is attributed to Li_7Sn_2 formation/decomposition resulting from the conversion reaction between intermetallic $\text{Ni}_{3,4}\text{Sn}_4$ and Li [17].

Regarding composites with constant C-amount (13wt.%) and increasing Si-content from 10 to 30 wt.%, the evolution of reversible capacity upon cycling is displayed in Fig. 8. Composites with 20 and 30 wt.% of Si exhibit reversible capacities close to 700 mAhg^{-1} at the third cycle whereas 10%-Si gives much lower capacity (388 mAhg^{-1}) for the same cycle. The capacity fading over 400 cycles is 0.077 and 0.082 %/cycle for 10 and 30 wt.% Si, respectively but only 0.039 %/cycle for 20 wt.% Si. Coulombic efficiencies have also been determined for the Si-series (Fig. S4, Supplementary Information). As for the C-series, they are close to 100%

without clear differences with the composition.

Fig. 9a shows the voltage profiles at the first galvanostatic cycle for the 10 and 30 wt.%-Si composites. For the first discharge, capacities of 794 mAhg^{-1} and 1186 mAhg^{-1} are achieved. Upon charge 572 mAhg^{-1} and 966 mAhg^{-1} are recovered, respectively. On discharge, the potential gradually drops down to 0.5 V for both composites followed by a pseudo-plateau down to 0 V, which is larger for the Si-rich composite. The irreversible capacity for the Si-poor composite (28%) is higher than that of the Si-rich one (17%). Fig. 9b shows the dQ/dV dependence vs potential for the two Si composites (10 and 30 wt.%) at the third cycle. The two redox pairs related to Si lithiation/delithiation at 0.22/0.49V and 0.09/0.34 V as well as that related to the conversion reaction of $\text{Ni}_{3,4}\text{Sn}_4$ at 0.3/0.62 V are observed. They concur with the three redox pairs observed in the carbon-series (Fig. 7b) leading to the formation/decomposition of $\text{LiSi-Li}_7\text{Si}_3$, $\text{Li}_{13}\text{Si}_4$ and Li_7Sn_2 . It is worth to note that for the composite with 30wt.%, in addition to 0.3/0.62 V redox pair, new peaks appear at higher potentials that are attributed to the formation of Li-poor Li_ySn alloys such as Li_5Sn_2 , Li_7Sn_3 and LiSn [17,42]. The peak intensity is significantly lower for the composite with lowest Si-content (10 wt.%) as concerns not only Li_ySi both also Li_ySn signals. The latter result implies that reversible lithiation of $\text{Ni}_{3,4}\text{Sn}_4$ intermetallic, which is the major phase for the Si-poor composite (Table 2), is very limited.

4. Discussion

Seven composites synthesized by mechanochemistry of four components (Si, $\text{Ni}_{3,4}\text{Sn}_4$, Al and C) have been prepared with different amounts of silicon (from 10 to 30 wt.%) and carbon (from 0 to 20 wt.%). After 20 hours of milling, all composites consist of a mixture of ~100 nm in size nanostructured Si particles surrounded by a matrix that is composed of several phases: $\text{Ni}_{3,4}\text{Sn}_4$, C, NiSi_2 and Sn. The phase amount and crystallinity of the constituents of this matrix

as well as its morphology depend both on C and Si-contents. As shown in Fig. 4, for high C-content (17 and 20 wt.%) and low Si-content (10 wt.%) the matrix is chemically heterogeneous at the spatial resolution of SEM-BSE analysis, showing large micrometric $\text{Ni}_{3.4}\text{Sn}_4$ areas. In contrast, for low C-content (9 and 13 wt.%) and high Si-content (20 and 30 wt.%), all matrix constituents are intimately mixed at the nanoscale and form a homogeneous matrix, mainly composed of $\text{Ni}_{3.4}\text{Sn}_4$ and disordered carbon, in which the Si nanoparticles are embedded. In the latter nanocomposites, crystallite sizes for Si and $\text{Ni}_{3.4}\text{Sn}_4$ remain in the low nanocrystalline range with $L_{\text{Si}} = 12 \pm 2$ nm and $L_{\text{Ni}_{3.4}\text{Sn}_4} = 8 \pm 1$ nm (Table 2).

Despite compositional and microstructural differences, the electrochemical voltage profiles are alike for all C-containing composites as regards to the reaction between Si and lithium (Fig. 7 & Fig. 9). In contrast, reversible lithiation of $\text{Ni}_{3.4}\text{Sn}_4$ is only detected when the intermetallic domains are small, *i.e.* when a homogenous matrix is formed. This concurs with previous studies on $\text{Ni}_{3.4}\text{Sn}_4$ nanostructuration [17], showing that micrometric $\text{Ni}_{3.4}\text{Sn}_4$ exhibits very limited reactivity with Li providing low reversible capacity (below 25 mAhg⁻¹), while nanometric one is much more reactive, reaching 240 mAhg⁻¹ for a crystallite size of 6 nm, comparable with present result (Table 2). Reactivity of both Si and $\text{Ni}_{3.4}\text{Sn}_4$ phases allows approaching the first lithiation capacity to the upper-limit capacity with ratio exceeding 95% (Table 3). The dQ/dV dependence *vs* potential curves confirms the reactivity of Si and $\text{Ni}_{3.4}\text{Sn}_4$ phases [43,44], being the latter only observed for low C contents and rich Si ones. Interestingly, when the intermetallic phase reacts (*i.e.* for homogenous matrix), the Si lithiation/delithiation peaks are broader (9 wt.% C in Fig. 7b). This can be tentatively attributed to the confinement effect of Si-lithiation by the surrounding matrix.

The present results clearly demonstrate that the Si/C ratio influences both microstructural and electrochemical properties. First, the role plaid by carbon for the phase stability and structuration of the composites at the milling stage is crucial. For the carbon-free composite,

silicon and $\text{Ni}_{3,4}\text{Sn}_4$ react according to R_1 and form tin and binary phase NiSi_2 . This reaction is detrimental for efficient composite nanostructuring on milling due to the high ductility of tin. Indeed, relatively large crystallite size is observed for Sn ($L_{\text{Sn}} = 27$ nm) in C-free composite. Moreover, as concerns electrochemical properties, NiSi_2 is reported to be inactive toward lithium [22] and tin may suffer from agglomeration effects on cycling [45]. These two latter properties are at the origin of the poor electrochemical cycling performance of C-free composite. These issues were solved by carbon addition: with 9 wt.% of carbon, Sn formation decreases from 42 wt.% down to 3.2 wt.%, meanwhile for 20 wt.% of carbon almost no tin formation occurs (0.7 wt.%). Thus, we demonstrate that carbon behaves as an efficient PCA agent: it prevents reaction R_1 by avoiding surface contact between Si and $\text{Ni}_{3,4}\text{Sn}_4$ powders.

Beside its PCA role on milling, carbon is known to have beneficial effects on electrochemical properties of Si-based electrodes enabling to accommodate volume changes and to insure good electronic conductivity [46,47]. However, it provides low electrochemical capacity as compared to silicon or tin. Therefore, carbon content should be optimized. Moreover, in the present investigation, it is observed that the amount of carbon is decisive to the formation of a homogeneous matrix embedding Si-nanoparticles. As mentioned earlier, for a constant Si-amount, this homogeneous matrix is efficiently formed at low C-contents (9 and 13 wt.%) but not at high C-ones (17 and 20 wt.%). Interestingly, the capacity fading in the C-series shows an inverse correlation with C-amount and therefore with the formation of the homogeneous matrix. Capacity fading gradually increases from 0.024 at 0.073 %/cycle when C-content increases from 9 to 20 wt.% (Table 3). This result empirically demonstrates that the homogeneous $\text{Ni}_{3,4}\text{Sn}_4$ -C matrix efficiently accommodates Si volume changes on cycling ensuring long cycle-life in composites Si- $\text{Ni}_{3,4}\text{Sn}_4$ -Al-C.

Beside carbon as milling PCA agent, conductive binder and matrix former, silicon plays a key electrochemical role as it provides most of the capacity for the composite. Formally,

increasing Si content should increase the capacity. This is indeed the case for the first lithiation of 10 and 20 wt.% of Si (at constant carbon amount of 13 wt.%) that provides 794 and 1191 mAhg⁻¹, respectively. However, increasing the Si amount to 30 wt.% does not bring further capacity and the first discharge capacity, 1186 mAhg⁻¹, remains far from the upper-limit capacity 1535 mAhg⁻¹. In fact, the 30wt.%-Si composite exhibits experimental capacities very similar to those of 20 wt.% Si (Table 3, Fig. 8). Several factors may account for this result. First, as the Si content increases from 10 to 30 wt.%, the amount of Ni_{3,4}Sn₄ decreases from 74 to 54 wt.%, reducing the efficiency of the latter phase to accommodate Si volume expansion. Second, when Si-content increases, the extent of reaction R₁ increases on milling and more NiSi₂ is formed (up to 6 wt.% for composite 30 wt.% Si). This partially consumes Si to produce electrochemically inactive NiSi₂.

To summarize, the highest electrochemical capacity with good cycle-life performances has been found for composite materials formed by Si-nanoparticles embedded in a homogenous Ni_{3,4}Sn₄-C matrix. This corresponds to C-contents in the range 9-13wt.% and Si-contents in the range 20-30 wt.%. Nanocomposites have reversible capacity that well exceeds that of graphite and allow to sustain reasonable cycle life for hundreds of cycles (Fig. 6 and Fig. 8).

5. Conclusion

Seven composites have been prepared by milling four components (Si, Ni_{3,4}Sn₄, Al and C) varying the amounts of silicon (10 to 30 wt.%) and carbon (0 to 20 wt.%). All composites contain Si nanoparticles surrounded by a nanostructured matrix made of Ni_{3,4}Sn₄, Sn, NiSi₂, disordered carbon and aluminum. This matrix is chemically homogeneous at the submicrometric level, and mainly consist of nanometric Ni_{3,4}Sn₄ and carbon, for C-contents in the range 9-13wt.% and Si-contents in the range 20-30 wt.%. The electrochemical profiles show that the reaction mechanism occurs in two main steps, i) the reaction of the intermetallic with

Li between 0.6 and 0.3 V to form Li_ySn phases and ii) the reaction of Li with silicon between 0.25 and 0.09 V to form Li_ySi phases. The formation of Li_ySn phases only occurs when the composite matrix contains nanometric $\text{Ni}_{3,4}\text{Sn}_4$. During milling, carbon addition prevents formation of Sn and NiSi_2 by impeding the reaction occurring between Si and $\text{Ni}_{3,4}\text{Sn}_4$. In addition, carbon in combination with $\text{Ni}_{3,4}\text{Sn}_4$ bring electronic conductivity and volume change accommodation of Si upon (de-)lithiation. However, carbon content should be limited to the range 9-13wt.% as higher content is detrimental to form a homogeneous $\text{Ni}_{3,4}\text{Sn}_4/\text{C}$ matrix that effectively accommodates Si volume changes during electrochemical cycling. As concerns silicon, higher amount brings better capacity, but a saturation is observed at 20 wt.%-Si with increased capacity fading upon cycling attributed to loss of strain accommodation and conductivity enhancement on reducing the amount of $\text{Ni}_{3,4}\text{Sn}_4/\text{C}$ matrix. An optimum Si/matrix ratio should be preserved to overcome these issues. Furthermore, this work supports previous studies suggesting that $\text{Ni}_{3,4}\text{Sn}_4$ needs to be highly nanostructured to provide significant reversible capacity and long-cycle-life [15,17,48], and demonstrates that, when used as a buffering matrix for Si-type anodes, it must form a homogenous matrix surrounding Si nanoparticles. Optimization of the electrode formulation and testing in full cell configuration are still needed to fully develop this anode materials for practical Li-ion batteries.

Acknowledgment

The authors are grateful to Remy PIRES for SEM and EDX analysis and to the French Research Agency ANR (project NEWMASTE, n°ANR-13-PRGE-0010) for financial support.

References

- [1] P.G. Bruce, S.A. Freunberger, L.J. Hardwick, J.-M. Tarascon, Li–O₂ and Li–S batteries with high energy storage, *Nat. Mater.* 11 (2012) 19–29. <https://doi.org/10.1038/nmat3191>.
- [2] O. Gröger, H.A. Gasteiger, J.-P. Suchsland, Review—Electromobility: Batteries or Fuel Cells?, *J. Electrochem. Soc.* 162 (2015) A2605–A2622. <https://doi.org/10.1149/2.0211514jes>.
- [3] P. Van den Bossche, F. Vergels, J. Van Mierlo, J. Matheys, W. Van Autenboer, SUBAT: An assessment of sustainable battery technology, *J. Power Sources.* 162 (2006) 913–919. <https://doi.org/10.1016/j.jpowsour.2005.07.039>.
- [4] S. Goriparti, E. Miele, F. De Angelis, E. Di Fabrizio, R. Proietti Zaccaria, C. Capiglia, Review on recent progress of nanostructured anode materials for Li-ion batteries, *J. Power Sources.* 257 (2014) 421–443. <https://doi.org/10.1016/j.jpowsour.2013.11.103>.
- [5] L. Croguennec, M.R. Palacin, Recent Achievements on Inorganic Electrode Materials for Lithium-Ion Batteries, *J. Am. Chem. Soc.* 137 (2015) 3140–3156. <https://doi.org/10.1021/ja507828x>.
- [6] S.-H. Yu, X. Feng, N. Zhang, J. Seok, H.D. Abruña, Understanding Conversion-Type Electrodes for Lithium Rechargeable Batteries, *Acc. Chem. Res.* 51 (2018) 273–281. <https://doi.org/10.1021/acs.accounts.7b00487>.
- [7] D. Larcher, S. Beattie, M. Morcrette, K. Edström, J.C. Jumas, J.M. Tarascon, Recent findings and prospects in the field of pure metals as negative electrodes for Li-ion batteries, *J. Mater. Chem.* 17 (2007) 3759–3772.
- [8] J.O. Besenhard, *Handbook of Battery Materials*, Wiley-VCH, 1998.
- [9] M.N. Obrovac, L. Christensen, Structural changes in silicon anodes during lithium insertion/extraction, *Electrochem. Solid-State Lett.* 7 (2012) A93–A94.
- [10] M.N. Obrovac, L.J. Krause, Reversible cycling of crystalline silicon powder, *J. Electrochem. Soc.* 154 (2007) A103–A108. <https://doi.org/10.1149/1.2402112>.
- [11] L. Beaulieu, K. Eberman, R. Turner, L. Krause, Colossal reversible volume changes in lithium alloys, *Electrochem. Solid State Lett.* 4 (2001) A137–A140. <https://doi.org/10.1149/1.1388178>.
- [12] X. Zuo, J. Zhu, P. Müller-Buschbaum, Y.-J. Cheng, Silicon based lithium-ion battery anodes: A chronicle perspective review, *Nano Energy.* 31 (2017) 113–143. <https://doi.org/10.1016/j.nanoen.2016.11.013>.
- [13] T. Song, K.C. Kil, Y. Jeon, S. Lee, W.C. Shin, B. Chung, K. Kwon, U. Paik, Nitridated Si-Ti-Ni alloy as an anode for Li rechargeable batteries, *J. Power Sources.* 253 (2014) 282–286. <https://doi.org/10.1016/j.jpowsour.2013.12.041>.
- [14] Z. Edfouf, F. Cuevas, M. Latroche, C. Georges, C. Jordy, T. Hezeque, G. Caillon, J.C. Jumas, M.T. Sougrati, Nanostructured Si/Sn-Ni/C composite as negative electrode for Li-ion batteries, *J. Power Sources.* 196 (2011) 4762–4768. <https://doi.org/10.1016/j.jpowsour.2011.01.046>.
- [15] H. Mukaibo, T. Mommaa, T. Osaka, Changes of electro-deposited Sn–Ni alloy thin film for lithium ion battery anodes during charge discharge cycling., *J. Power Sources.* 146 (2005) 457–463.
- [16] S. Naille, R. Dedryvère, D. Zitoun, P.E. Lippens, Atomic scale characterization of tin based intermetallic anodes, *J. Power Sources.* 189 (2009) 806–808.
- [17] Z. Edfouf, C. Fariaut-Georges, F. Cuevas, M. Latroche, T. Hézèque, G. Caillon, C. Jordy, M.T. Sougrati, J.C. Jumas, Nanostructured Ni_{3,5}Sn₄ intermetallic compound: an efficient buffering material for Si containing composite anodes in lithium ion batteries,

- Electrochimica Acta. 89 (2013) 365–371.
<https://doi.org/10.1016/j.electacta.2012.11.078>.
- [18] A. Kitada, N. Fukuda, T. Ichii, H. Sugimura, K. Murase, Lithiation behavior of single-phase Cu-Sn intermetallics and effects on their negative-electrode properties, *Electrochem. Acta.* 98 (2013) 239–243. <https://doi.org/10.1016/j.electacta.2013.03.035>.
- [19] R. Alcántara, J.L. Tirado, J.-C. Jumas, L. Monconduit, J. Olivier-Fourcade, Electrochemical reaction of lithium with CoP₃, *J. Power Sources.* 109 (2002) 308–312.
- [20] S. Wang, M. He, M. Walter, F. Krumeich, K.V. Kravchyk, M.V. Kovalenko, Monodisperse CoSn₂ and FeSn₂ nanocrystals as high-performance anode materials for lithium-ion batteries, *Nanoscale.* 10 (2018) 6827–6831.
<https://doi.org/10.1039/C7NR08261D>.
- [21] M. Gao, D. Wang, X. Zhang, H. Pan, Y. Liu, C. Liang, C. Shang, Z. Guo, A hybrid Si@FeSi_y/SiO_x anode structure for high performance lithium-ion batteries via ammonia-assisted one-pot synthesis, *J. Mater. Chem. A.* 3 (2015) 10767–10776.
<https://doi.org/10.1039/C5TA01251A>.
- [22] Z. Wang, W.H. Tian, X.H. Liu, Y. Li, X.G. Li, Nanosized Si–Ni alloys anode prepared by hydrogen plasma–metal reaction for secondary lithium batteries, *Mater. Chem. Phys.* 100 (2006) 92–97. <https://doi.org/10.1016/j.matchemphys.2005.12.011>.
- [23] S.-B. Son, S.C. Kim, C.S. Kang, T.A. Yersak, Y.-C. Kim, C.-G. Lee, S.-H. Moon, J.S. Cho, J.-T. Moon, K.H. Oh, S.-H. Lee, A Highly Reversible Nano-Si Anode Enabled by Mechanical Confinement in an Electrochemically Activated Li_xTi₄Ni₄Si₇ Matrix, *Adv. Energy Mater.* 2 (2012) 1226–1231. <https://doi.org/10.1002/aenm.201200180>.
- [24] J.-S. Cho, P.K. Alaboina, C.-S. Kang, S.-C. Kim, S.-B. Son, S. Suh, J. Kim, S. Kwon, S.-H. Lee, K.-H. Oh, S.-J. Cho, Ex Situ Investigation of Anisotropic Interconnection in Silicon-Titanium-Nickel Alloy Anode Material, *J. Electrochem. Soc.* 164 (2017) A968.
<https://doi.org/10.1149/2.0221706jes>.
- [25] H.-I. Park, M. Sohn, J.-H. Choi, C. Park, J.-H. Kim, H. Kim, Microstructural Tuning of Si/TiFeSi₂ Nanocomposite as Lithium Storage Materials by Mechanical Deformation, *Electrochimica Acta.* 210 (2016) 301–307.
<https://doi.org/10.1016/j.electacta.2016.05.168>.
- [26] Z. Dong, H. Gu, W. Du, Z. Feng, C. Zhang, Y. Jiang, T. Zhu, G. Chen, J. Chen, Y. Liu, M. Gao, H. Pan, Si/Ti₃SiC₂ composite anode with enhanced elastic modulus and high electronic conductivity for lithium-ion batteries, *J. Power Sources.* 431 (2019) 55–62.
<https://doi.org/10.1016/j.jpowsour.2019.05.043>.
- [27] Y. Chen, J. Qian, Y. Cao, H. Yang, X. Ai, Green Synthesis and Stable Li-Storage Performance of FeSi₂/Si@C Nanocomposite for Lithium-Ion Batteries, *ACS Appl. Mater. Interfaces.* 4 (2012) 3753–3758. <https://doi.org/10.1021/am300952b>.
- [28] S.-S. Lee, K.-H. Nam, H. Jung, C.-M. Park, Si-based composite interconnected by multiple matrices for high-performance Li-ion battery anodes, *Chem. Eng. J.* 381 (2020) 122619. <https://doi.org/10.1016/j.cej.2019.122619>.
- [29] C. Jordy, G. Caillon, T. Hézèque, C. Audry, F. Cuevas, M. Latroche, Active material composition for the negative electrode of a lithium-ion accumulator, EP2239803, US 2010270497, 2010.
- [30] T.D. Hatchard, J.M. Toppole, M.D. Fleischauer, J.R. Dahn, Electrochemical performance of SiAlSn films prepared by combinatorial sputtering, *Electrochem. Solid-State Lett.* 6 (2003) A129–A132.
- [31] Z. Edfouf, F. Cuevas, M. Latroche, C. Georges, C. Jordy, G. Caillon, T. Hézèque, J.-C. Jumas, M.T. Sougrati, Nanostructured Si/Sn–Ni/C composite as negative electrode for Li-ion batteries, *J. Power Sources.* 196 (2011) 4762–4768.

- [32] Z. Edfouf, M.T. Sougrati, C. Fariaut-Georges, F. Cuevas, J.-C. Jumas, T. Hézèque, C. Jordy, G. Caillon, M. Latroche, Reactivity assessment of lithium with the different components of novel Si/Ni_{3.4}Sn₄/Al/C composite anode for Li-ion batteries, *J. Power Sources*. 238 (2013) 210–217. <https://doi.org/10.1016/j.jpowsour.2013.01.197>.
- [33] J. Rodriguez-Carvajal, Fullprof: a program for Rietveld refinement and pattern matching analysis, *Phys. B*. 192 (1993) 55–69.
- [34] J.R. Ares, F. Cuevas, A. Percheron-Guégan, Mechanical milling and subsequent annealing effects on the microstructural and hydrogenation properties of multisubstituted LaNi₅ alloy, *Acta Mater.* 53 (2005) 2157–2167. <https://doi.org/10.1016/j.actamat.2005.01.030>.
- [35] S. Furuseth, H. Fjellvag, Structural Properties of Ni_{3+x}Sn₄, *Acta Chem. Scand. A* 40 (1986) 695–700.
- [36] P. Villar, K. Cenzual, Pearson's Crystal data: crystal structure database for inorganic compounds, release 2010/2011, ASM international, Materials Park, Ohio, USA, 2010.
- [37] C.K. Chan, H. Peng, G. Liu, K. McIlwrath, X.F. Zhang, R.A. Huggins, Y. Cui, High-performance lithium battery anodes using silicon nanowires, *Nat. Nanotechnol.* 3 (2008) 31–35.
- [38] B.-C. Yu, Y. Hwa, J.-H. Kim, H.-J. Sohn, Characterizations and electrochemical behaviors of milled Si with a degree of amorphization and its composite for Li-ion batteries, *J. Power Sources*. 260 (2014) 174–179. <https://doi.org/10.1016/j.jpowsour.2014.02.109>.
- [39] A. Reyes Jiménez, R. Klöpsch, R. Wagner, U.C. Rodehorst, M. Kolek, R. Nölle, M. Winter, T. Placke, A Step toward High-Energy Silicon-Based Thin Film Lithium Ion Batteries, *ACS Nano*. 11 (2017) 4731–4744. <https://doi.org/10.1021/acsnano.7b00922>.
- [40] M.-S. Park, Y.-J. Lee, S. Rajendran, M.-S. Song, H.-S. Kim, J.-Y. Lee, Electrochemical properties of Si/Ni alloy–graphite composite as an anode material for Li-ion batteries, *Electrochimica Acta*. 50 (2005) 5561–5567. <https://doi.org/10.1016/j.electacta.2005.04.042>.
- [41] W. Wang, P.N. Kumta, Reversible high capacity nanocomposite anodes of Si/C/SWNTs for rechargeable Li-ion batteries, *J. Power Sources*. 172 (2007) 650–658. <https://doi.org/10.1016/j.jpowsour.2007.05.025>.
- [42] Z. Chen, Y. Cao, J. Qian, X. Ai, H. Yang, Facile synthesis and stable lithium storage performances of Sn- sandwiched nanoparticles as a high capacity anode material for rechargeable Li batteries, *J. Mater. Chem.* 20 (2010) 7266–7271. <https://doi.org/10.1039/C0JM00829J>.
- [43] K.K.D. Ehinon, S. Naille, R. Dedryvère, P.-E. Lippens, J.-C. Jumas, D. Gonbeau, Ni₃Sn₄ Electrodes for Li-Ion Batteries: Li-Sn Alloying Process and Electrode/Electrolyte Interface Phenomena, *Chem. Mater.* 20 (2008) 5388–5398.
- [44] H. Wu, Y. Cui, Designing nanostructured Si anodes for high energy lithium ion batteries, *Nano Today*. 7 (2012) 414–429. <https://doi.org/10.1016/j.nantod.2012.08.004>.
- [45] Y. Kwon, M.G. Kim, Y. Kim, Y. Lee, J. Cho, Effect of Capping Agents in Tin Nanoparticles on Electrochemical Cycling, *Electrochem. Solid-State Lett.* 9 (2006) A34–A38. <https://doi.org/10.1149/1.2138447>.
- [46] T. Zhang, J. Gao, L.J. Fu, L.C. Yang, Y.P. Wu, H.Q. Wu, Natural graphite coated by Si nanoparticles as anode materials for lithium ion batteries, *J. Mater. Chem.* 17 (2007) 1321–1325. <https://doi.org/10.1039/B612967F>.
- [47] Z. Zhou, Y. Xu, W. Liu, L. Niu, High capacity Si/DC/MWCNTs nanocomposite anode materials for lithium ion batteries, *J. Alloys Compd.* 493 (2010) 636–639. <https://doi.org/10.1016/j.jallcom.2009.12.171>.

- [48] J. Hassoun, S. Panero, P. Simon, P.L. Taberna, B. Scrosati, High-Rate, Long-Life Ni–Sn Nanostructured Electrodes for Lithium-Ion Batteries, *Adv. Mater.* 19 (2007) 1632–1635. <https://doi.org/10.1002/adma.200602035>.

Table and figure captions

Table 1. Composition (in wt.%) of Si-Ni-Sn-Al-C composites milled 20 hours with different carbon and silicon contents

Table 2. Crystallographic data for nanostructured composites. Ni over-stoichiometry (x) in $\text{Ni}_{3+x}\text{Sn}_4$ and crystallite size (L) for all phases are given. Standard deviations referred to the last digit are given in parenthesis.

Table 3. Electrochemical properties for the composites milled 20 hours with different carbon and silicon contents. $C_{\text{upper-limit}}$ stands for the maximum expected capacity, $C_{\text{lith,1st}}$ and $C_{\text{delith,1st}}$ are the lithiation and delithiation capacities at first cycle, $C_{\text{irrev,1st}}$ is the irreversible capacity at first cycle and $C_{\text{rev,3rd}}$ and $C_{\text{rev,1000th}}$ are the reversible capacities at cycles 3 and 1000.

Fig. 1. XRD patterns of the carbon-free composite before (bottom) and after (top) 20h of milling. Position of diffraction lines for Sn, Si, NiSi_2 and $\text{Ni}_{3.4}\text{Sn}_4$ phases as reported in Pearson's crystal data base [36] are shown in the bottom part of the figure.

Fig. 2. XRD patterns for 20 wt.% Si composites with C-content varying from 9 wt.% (bottom) to 20wt.% (top).

Fig. 3. XRD patterns for 13 wt.% C composites and Si-content varying from 10 wt.% (bottom) to 30 wt.% (top).

Fig. 4. SEM-BSE cross section micrographs of the carbon-containing composites milled for 20 hours.

Fig. 5. SEM-BSE image (left) of the 9 wt.% C - 20 wt.% Si composite showing three different compositional areas. EDX point analyses of the three areas are displayed on the right-hand side.

Fig. 6. Reversible capacity on cycling for the four composites at constant Si-amount (20 wt.%) and increasing carbon content from 9 to 20 wt.%. Only reference cycles are shown. The first point corresponds to cycle 3 considered as the first reference cycle after two initial activation cycles.

Fig. 7. Profiles of the first galvanostatic cycles (a) and dQ/dV dependence as a function of voltage for the third cycle (b) for the 9 wt.% and 20wt. % carbon-containing composites. (Si-content = 20 wt.%).

Fig. 8. Reversible capacity on cycling for the composites with constant C-amount (13wt.%) and increasing Si-content from 10 to 30 wt.%. Only reference cycles are shown. The first point corresponds to cycle 3 considered as the first reference cycle after two initial activation cycles.

Fig. 9. Profiles of the first galvanostatic cycles (a) and dQ/dV dependence as a function of voltage for the third cycle (b) for the 10 wt.% and 30 wt.% silicon-containing composites (C-content = 13 wt.%).

Table 1

	10 wt.% Si	20 wt.% Si	30 wt.% Si
0 wt.% C		$\text{Si}_{0.22}\text{Ni}_{0.22}\text{Sn}_{0.53}\text{Al}_{0.03}$	
9 wt.% C		$\text{Si}_{0.20}\text{Ni}_{0.20}\text{Sn}_{0.48}\text{Al}_{0.03}\text{C}_{0.09}$	
13 wt.% C	$\text{Si}_{0.10}\text{Ni}_{0.22}\text{Sn}_{0.52}\text{Al}_{0.03}\text{C}_{0.13}$	$\text{Si}_{0.19}\text{Ni}_{0.19}\text{Sn}_{0.46}\text{Al}_{0.03}\text{C}_{0.13}$	$\text{Si}_{0.30}\text{Ni}_{0.16}\text{Sn}_{0.38}\text{Al}_{0.03}\text{C}_{0.13}$
17 wt.% C		$\text{Si}_{0.18}\text{Ni}_{0.18}\text{Sn}_{0.44}\text{Al}_{0.03}\text{C}_{0.17}$	
20 wt.% C		$\text{Si}_{0.18}\text{Ni}_{0.18}\text{Sn}_{0.42}\text{Al}_{0.03}\text{C}_{0.20}$	

Table 2

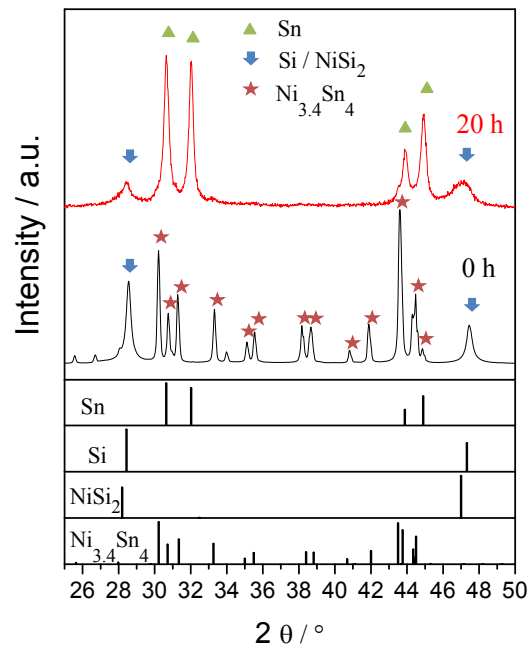
Composition C (wt%)	Si (wt%)	Phase	Content (wt.%)	S.G.	$a(\text{\AA})$	Cell parameters $b(\text{\AA})$	$c(\text{\AA})$	$\beta(^{\circ})$	x values $\text{Ni}_{3+x}\text{Sn}_4$	L (nm)
0	20	$\text{Ni}_{3+x}\text{Sn}_4$	9 (1)	$C2/m$	12.199*	4.0609*	5.2238*	105.17*	0.1*	10*
		Si	13 (1)	$Fd-3m$	5.430*					15 (2)
		Sn	43 (1)	$I4_1/amd$	5.8303 (2)		3.1822 (1)			27 (1)
		NiSi_2	35 (2)	$Fm-3m$	5.4731 (5)					5 (1)
9	20	$\text{Ni}_{3+x}\text{Sn}_4$	79(1)	$C2/m$	12.273 (1)	4.0421 (4)	5.2007 (5)	104.73 (1)	0.29 (3)	8 (1)
		Si	14 (1)	$Fd-3m$	5.430*					14 (2)
		Sn	3.2 (2)	$I4_1/amd$	5.830*		3.182*			22*
		NiSi_2	4 (1)	$Fm-3m$	5.470*					6*
13	20	$\text{Ni}_{3+x}\text{Sn}_4$	75 (1)	$C2/m$	12.299 (1)	4.0497 (3)	5.2043 (4)	104.67 (1)	0.29 (3)	8 (1)
		Si	17 (1)	$Fd-3m$	5.430*					14 (1)
		Sn	2.5 (4)	$I4_1/amd$	5.830*		3.182*			22*
		NiSi_2	5 (1)	$Fm-3m$	5.470*					6*
17	20	$\text{Ni}_{3+x}\text{Sn}_4$	74 (1)	$C2/m$	12.410 (1)	4.0685 (3)	5.2010 (6)	104.04 (1)	0.48 (3)	8 (1)
		Si	22 (1)	$Fd-3m$	5.430*					14 (1)
		Sn	0.9 (2)	$I4_1/amd$	5.830*		3.182*			22*
		NiSi_2	2 (1)	$Fm-3m$	5.470*					6*
20	20	$\text{Ni}_{3+x}\text{Sn}_4$	72 (1)	$C2/m$	12.452 (1)	4.0800 (1)	5.2089 (2)	103.60 (1)	0.60 (3)	50 (3)
		Si	27 (1)	$Fd-3m$	5.430*					17 (2)
		Sn	0.7 (2)	$I4_1/amd$	5.830*		3.182*			22*
		NiSi_2	0 (1)	$Fm-3m$	5.470*					6*
13	10	$\text{Ni}_{3+x}\text{Sn}_4$	90 (2)	$C2/m$	12.392 (2)	4.0679 (4)	5.1994 (6)	104.18 (1)	0.47 (3)	9 (1)
		Si	9 (1)	$Fd-3m$	5.430*					14 (3)
		Sn	0.5 (2)	$I4_1/amd$	5.830*		3.182*			22*
		NiSi_2	0 (1)	$Fm-3m$	5.470*					6*
13	30	$\text{Ni}_{3+x}\text{Sn}_4$	57 (2)	$C2/m$	12.287(2)	4.0466(6)	5.2079(8)	104.65(1)	0.37 (5)	7 (1)
		Si	31 (1)	$Fd-3m$	5.430*					11 (2)
		Sn	6 (0.3)	$I4_1/amd$	5.830*		3.182*			22*
		NiSi_2	6 (1)	$Fm-3m$	5.470*					6*

*Values were fixed to ensure refinement stability due to strong peak overlapping (Si and NiSi_2 phases) or low phase amount

Table 3

C/Si (wt.%)	$C_{\text{upper-limit}}$ (mAh g ⁻¹)	$C_{\text{lith,1st}}$ (mAhg ⁻¹)	$C_{\text{lith,1st}} / C_{\text{upper-limit}}$ (%)	$C_{\text{delith,1st}}$ (mAhg ⁻¹)	$C_{\text{irrev,1st}}$ (%)	$C_{\text{rev, 3rd}}$ (mAhg ⁻¹)	$C_{\text{rev, 1000th}}$ (mAhg ⁻¹)	Capacity fade (%/cycle)*
0/20	1348	949	70	716	25	510	213 ^a	0.28 ^a
9/20	1260	1196	95	985	18	707	542	0.024
13/20	1219	1191	98	1008	15	698	429	0.039
17/20	1178	1146	97	956	17	711	311	0.056
20/20	1170	923	79	702	24	522	136	0.073
13/10	955	794	83	572	28	388	256 ^b	0.077 ^b
13/30	1535	1186	77	966	17	700	487 ^c	0.082 ^c

*Fading values are calculated from cycle 3 to cycle 1000 except for *a*, *b* and *c* compositions for which last measured cycle was 206, 450 and 372, respectively.

**Fig. 1.**

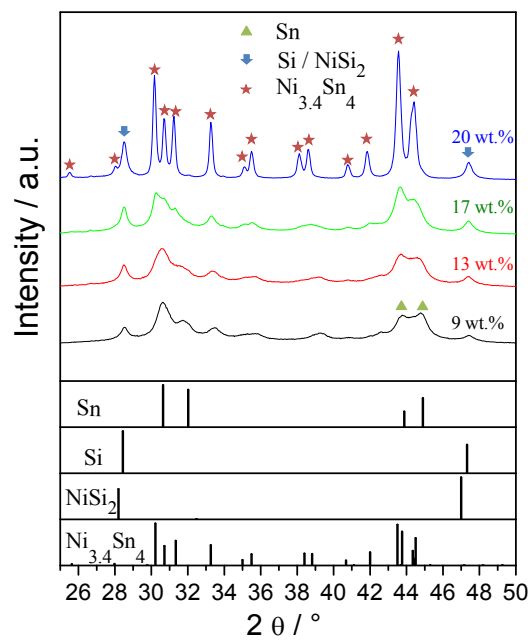


Fig. 2.

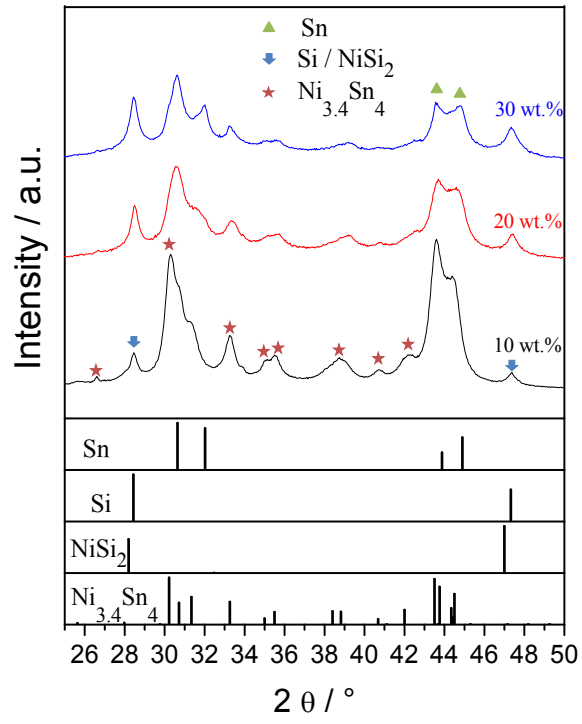


Fig. 3.

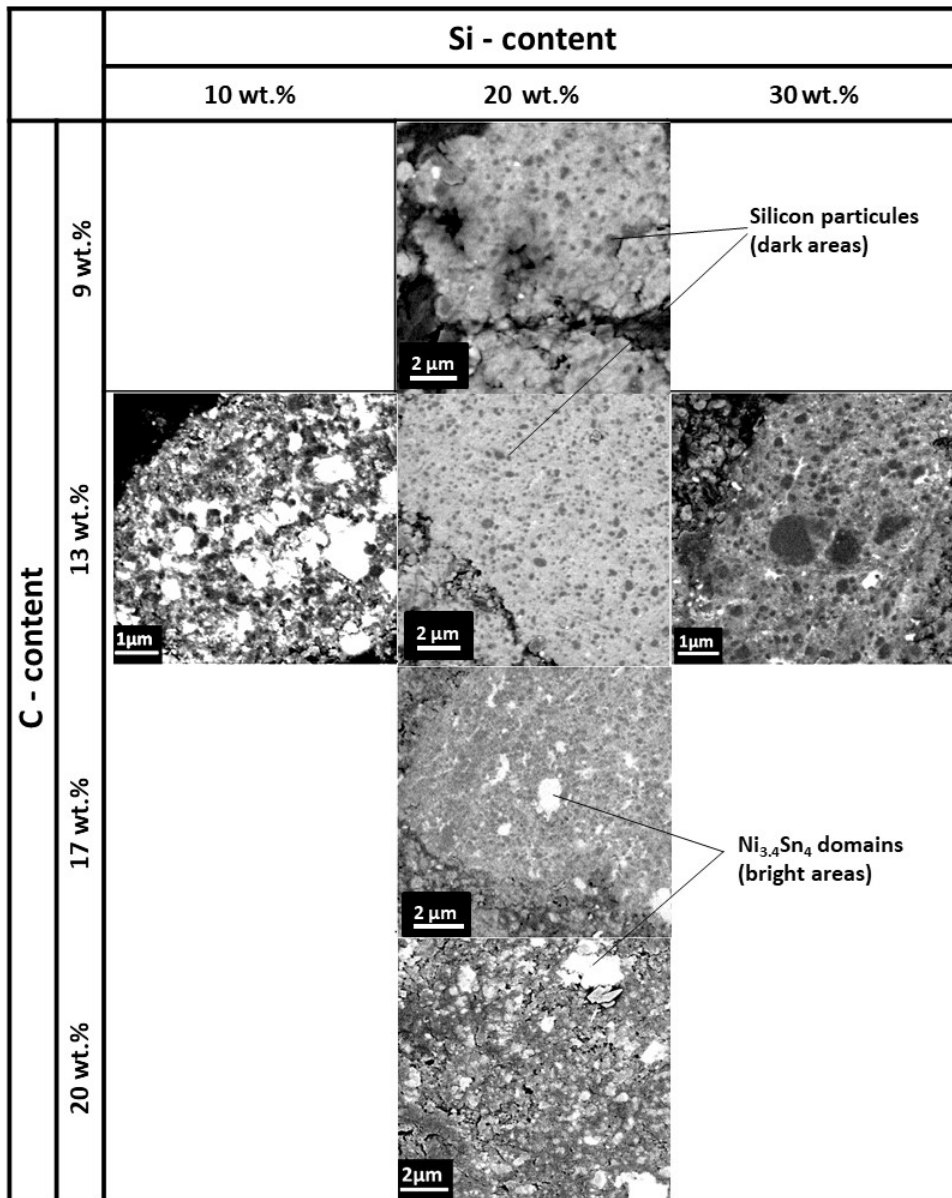


Fig. 4.

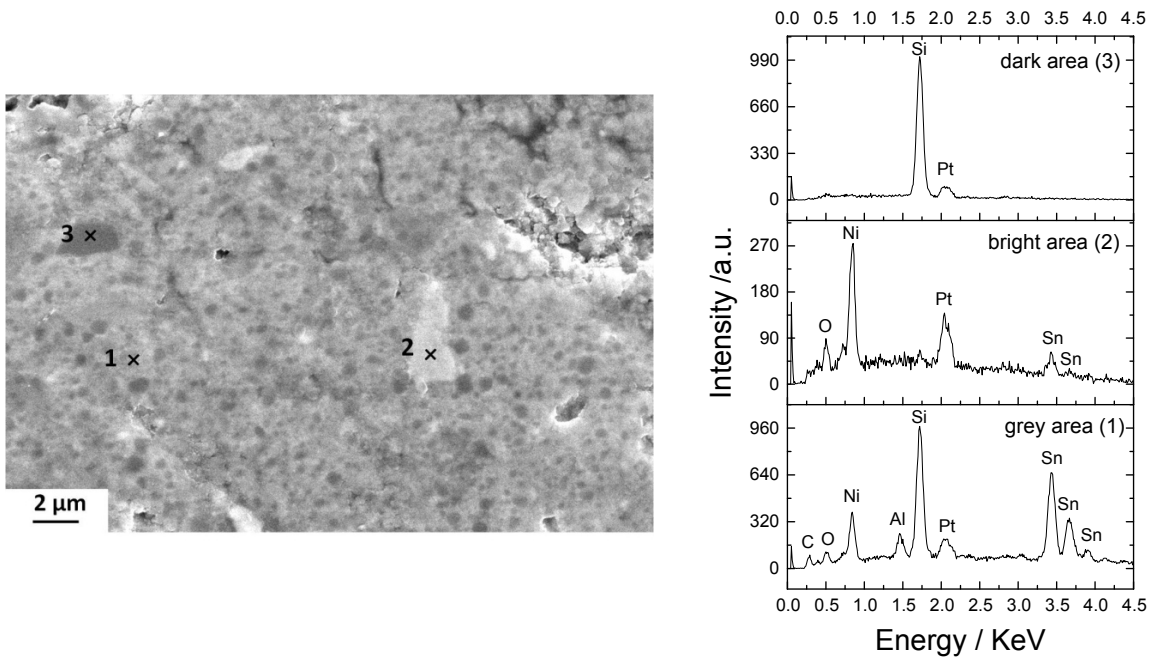


Fig. 5.

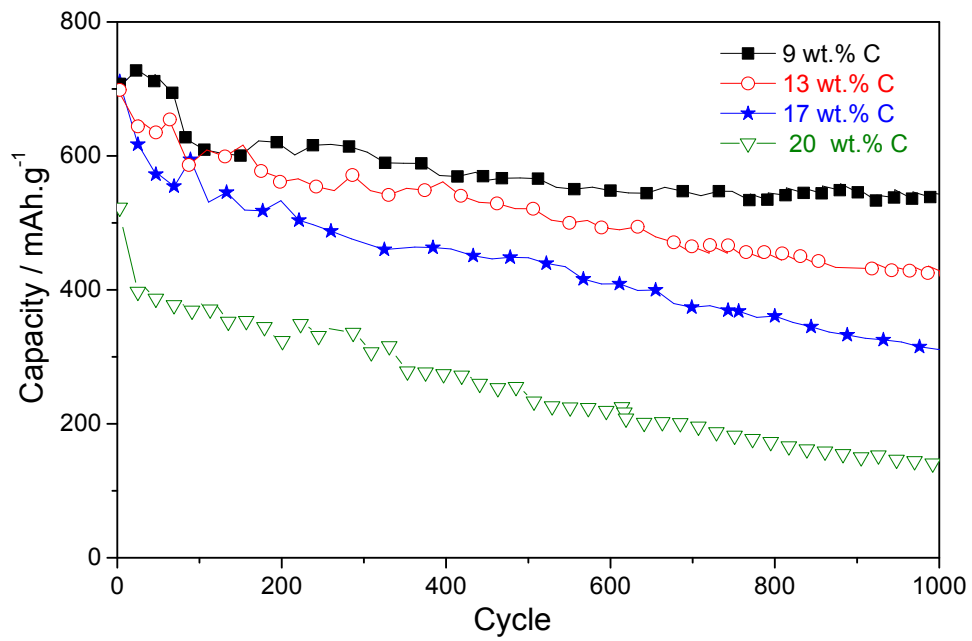


Fig. 6.

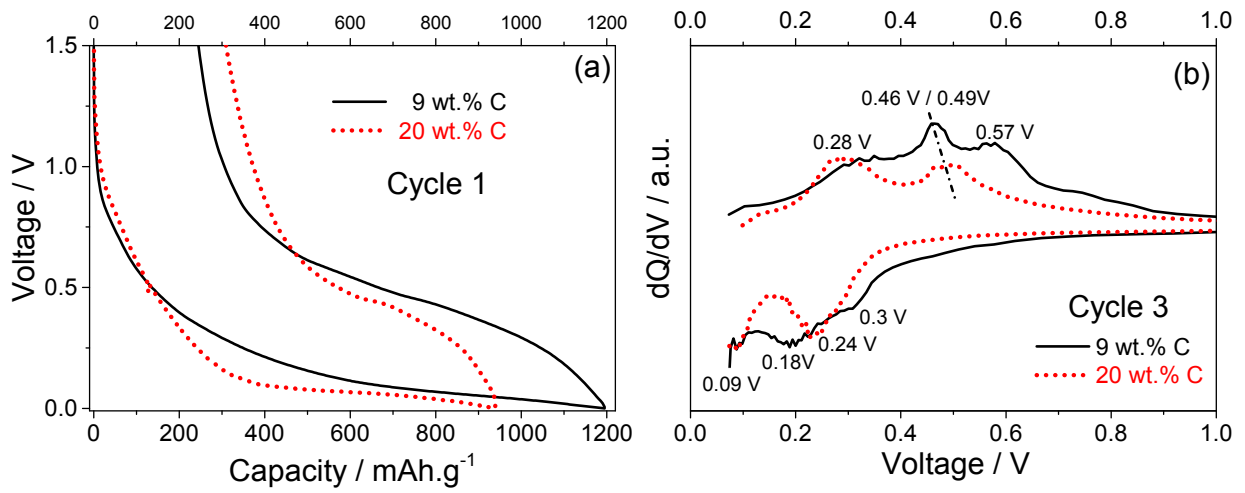
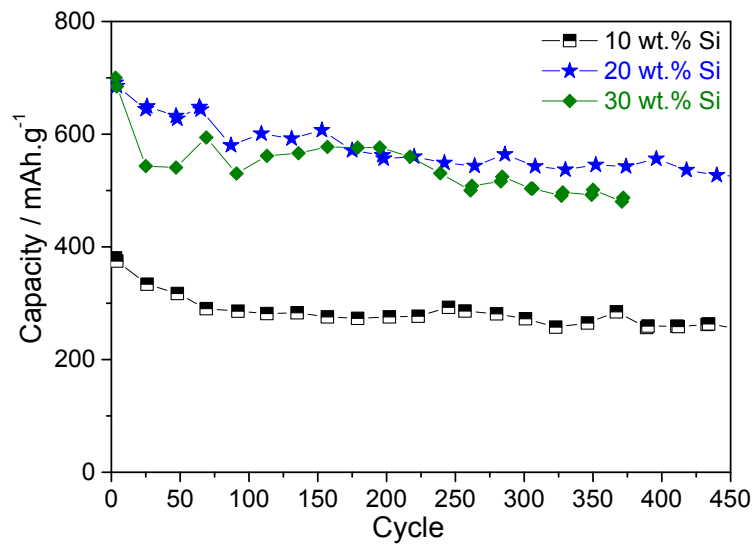


Fig. 7.

Fig. 8.



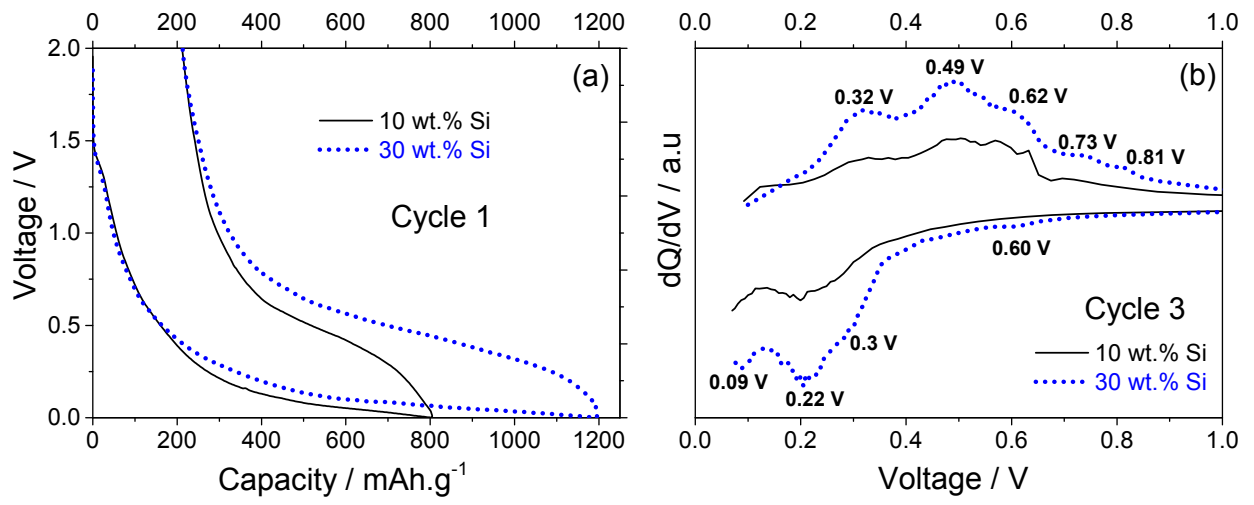


Fig. 9.

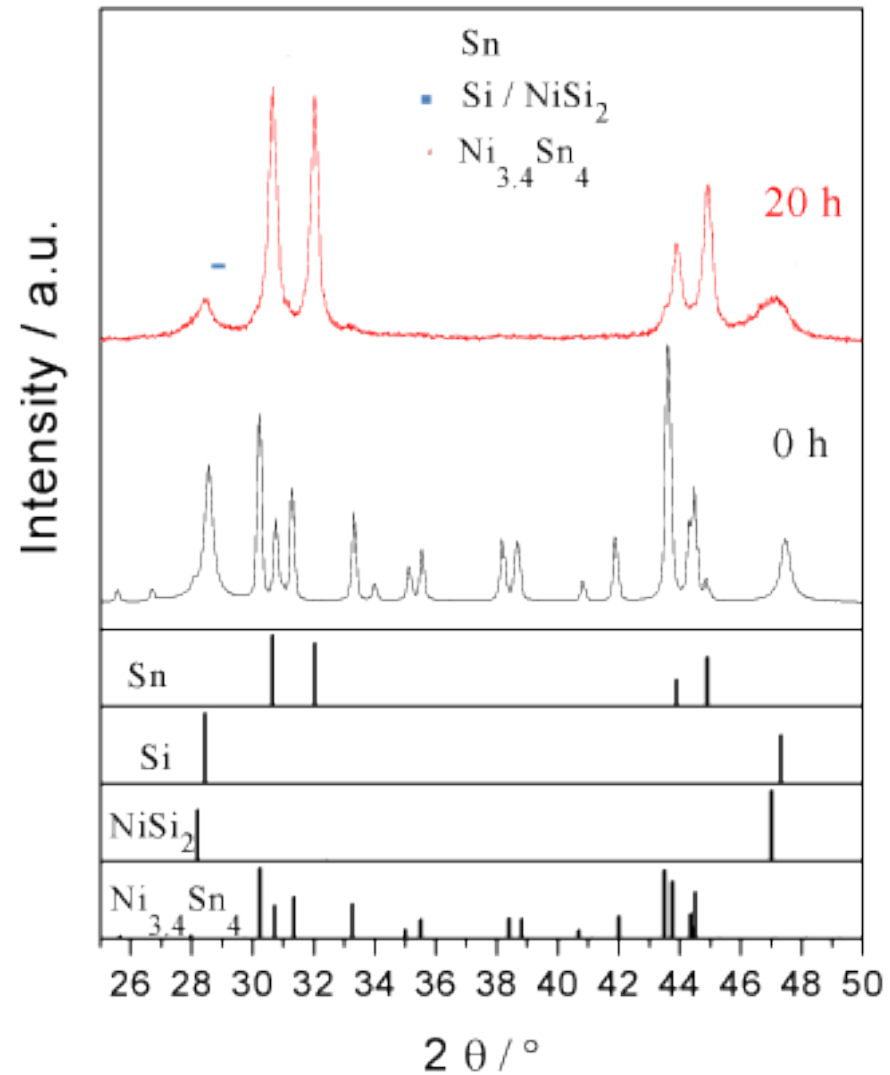


Fig. 1. XRD patterns of the carbon-free composite before (bottom) and after (top) 20h of milling. Position of diffraction lines for Sn, Si, NiSi₂ and Ni_{3.4}Sn₄ phases as reported in Pearson's crystal data base (Villar and Cenzual, 2010) are shown in the bottom part of the figure.

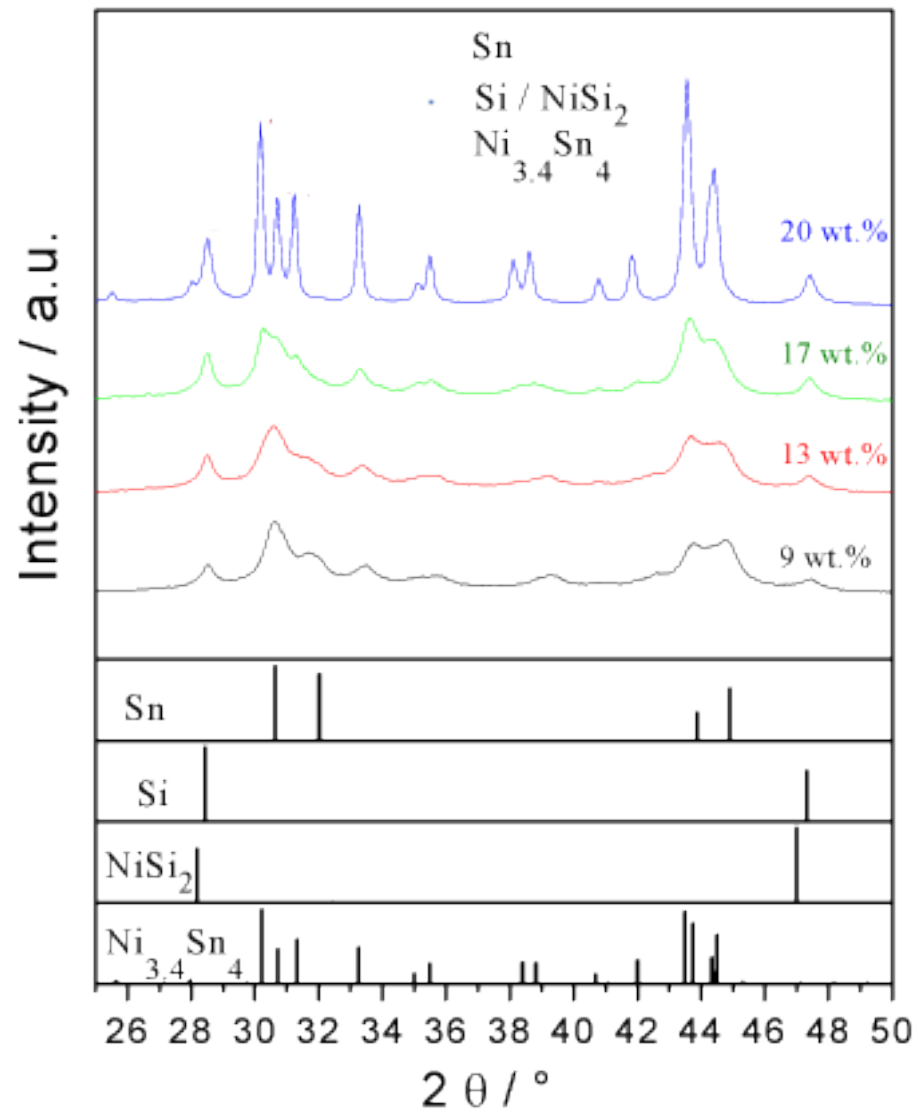


Fig. 2. XRD patterns for 20 wt.% Si composites with C-content varying from 9 wt.% (bottom) to 20 wt.% (top).

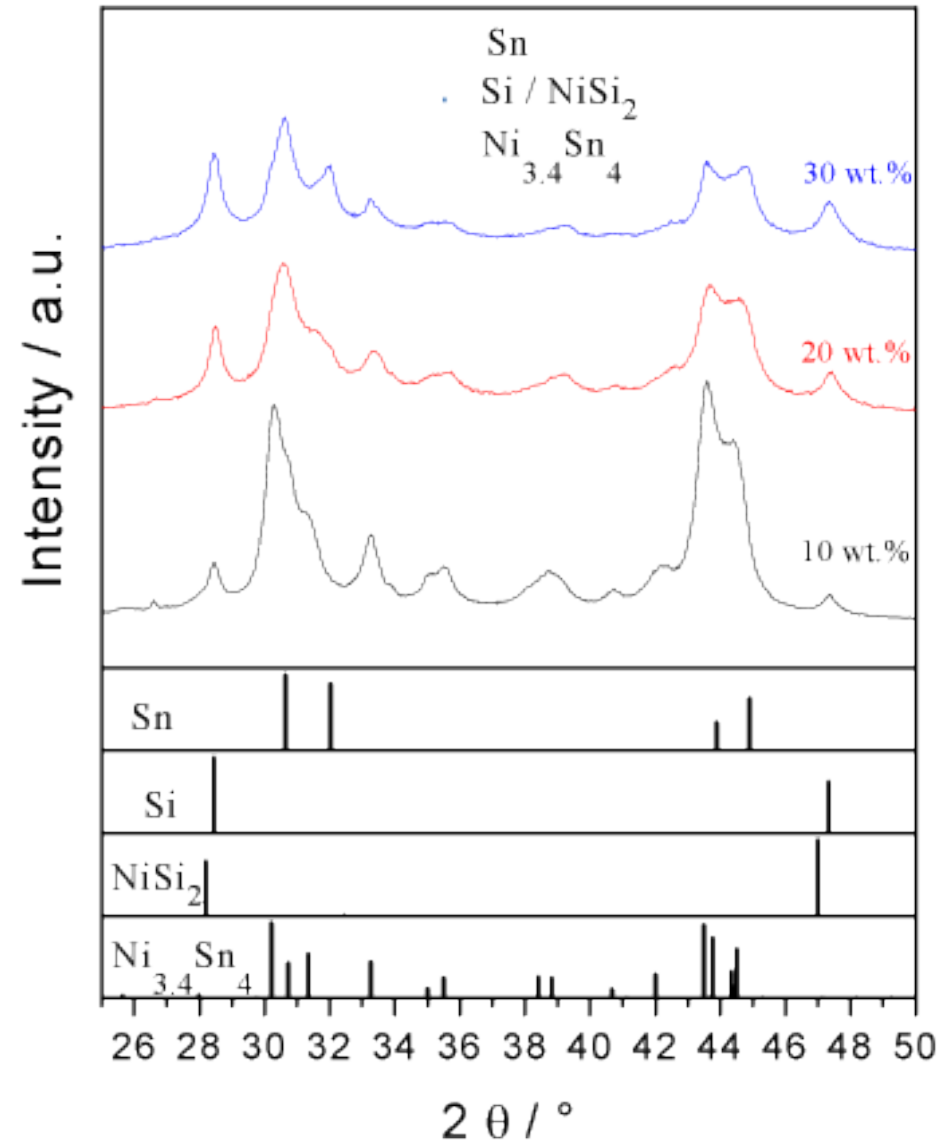


Fig. 3. XRD patterns for 13 wt.% C composites and Si-content varying from 10 wt.% (bottom) to 30 wt.% (top).

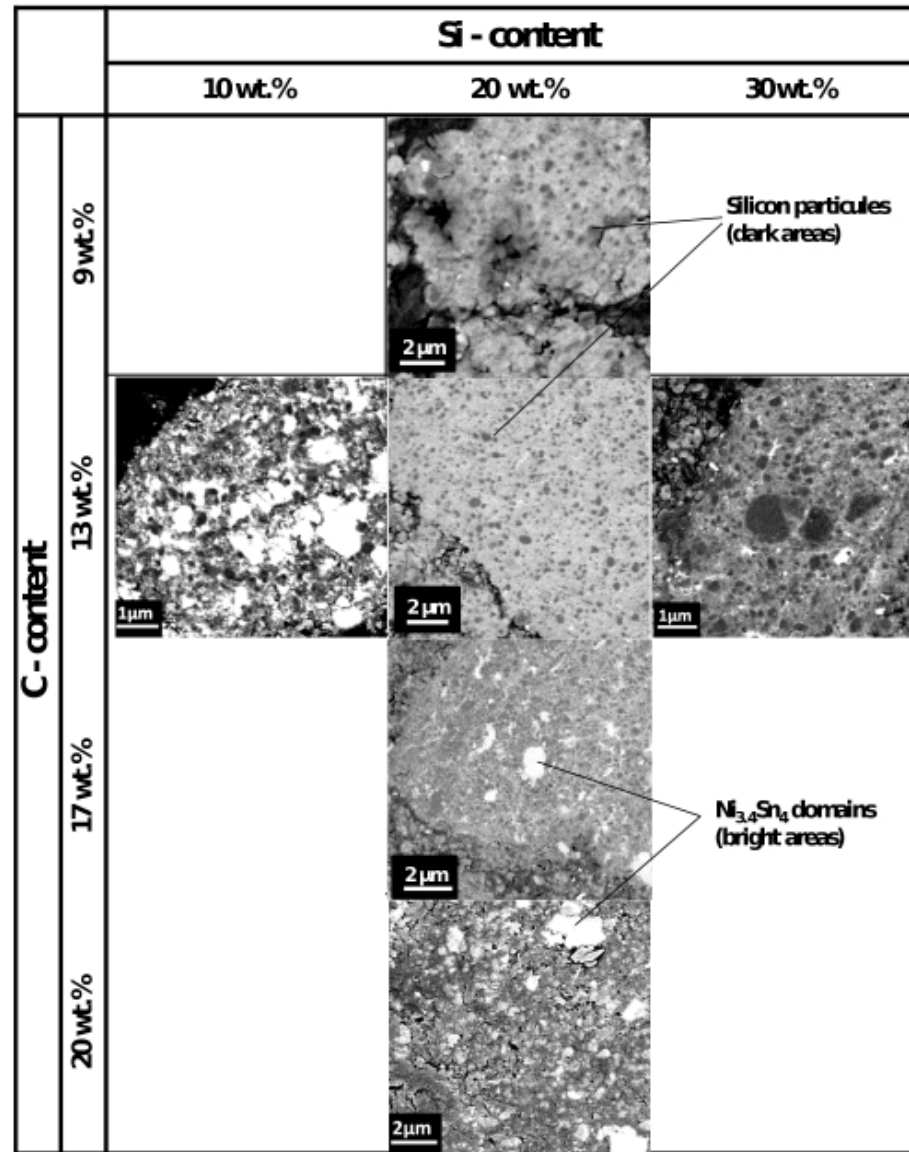


Fig. 4. SEM-BSE cross section micrographs of the carbon-containing composites milled for 20 hours.

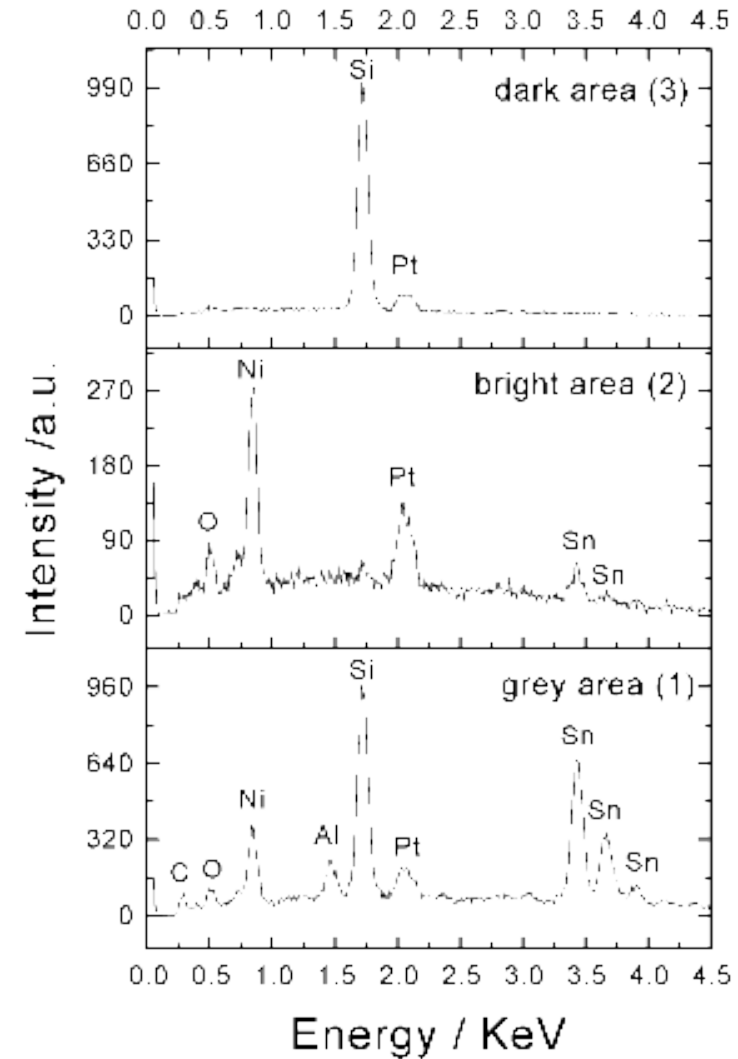
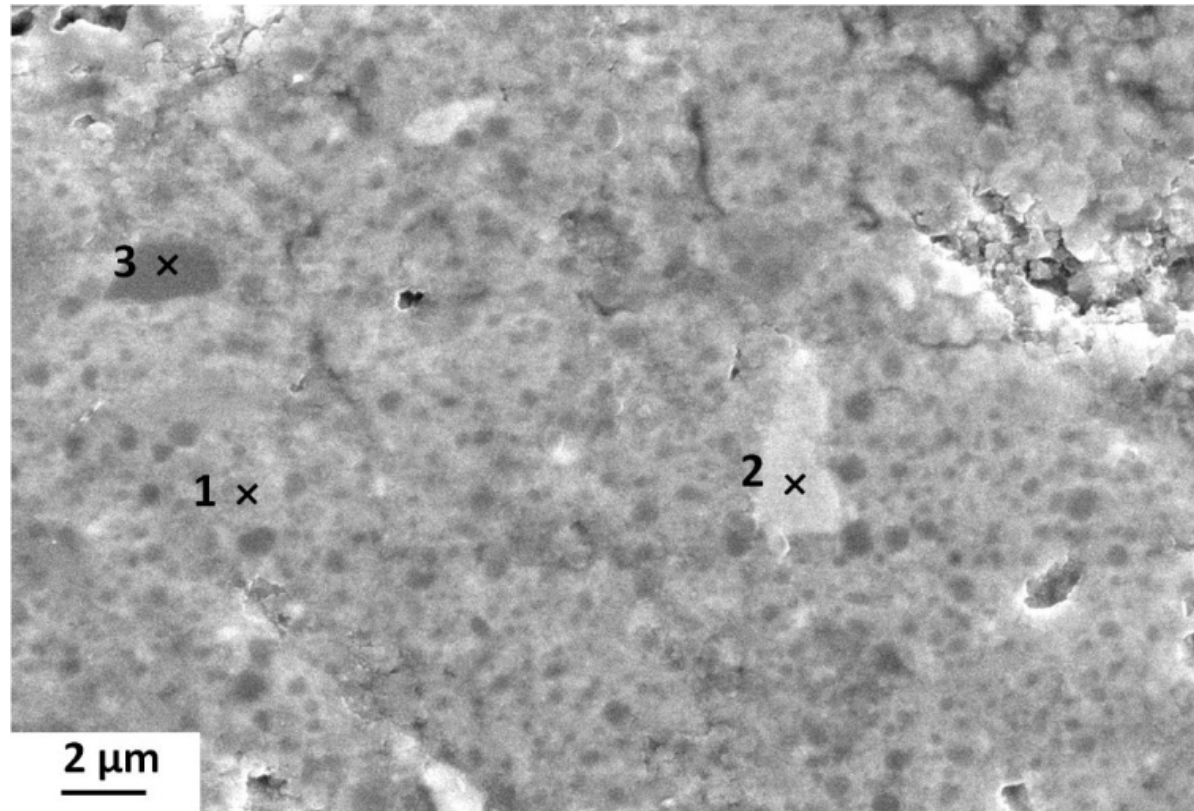


Fig. 5. SEM-BSE image (left) of the 9 wt.% C - 20 wt.% Si composite showing three different compositional areas. EDX point analyses of the three areas are displayed on the right-hand side.

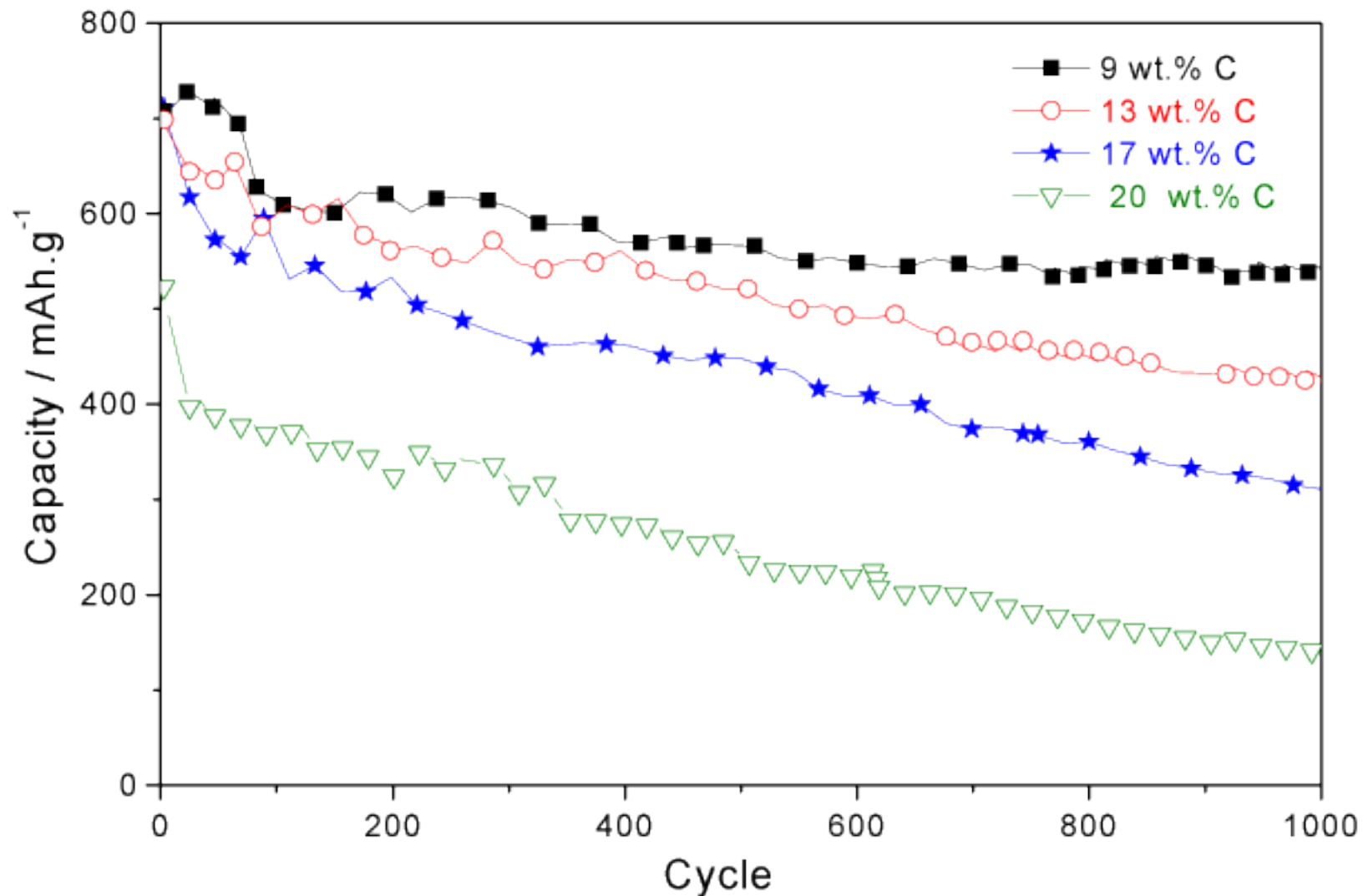


Fig. 6. Reversible capacity on cycling for the four composites at constant Si-amount (20 wt.%) and increasing carbon content from 9 to 20 wt.%. Only reference cycles are shown. The first point corresponds to cycle 3 considered as the first reference cycle after two initial activation cycles.

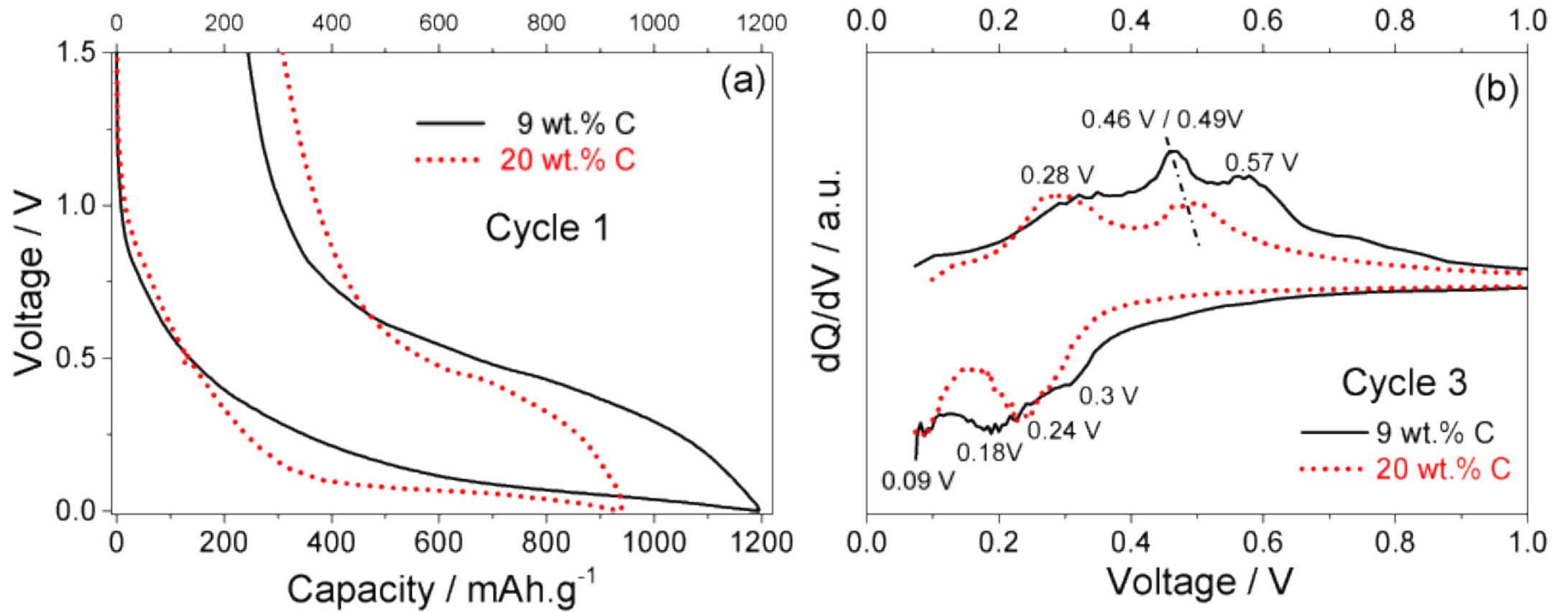


Fig. 7. Profiles of the first galvanostatic cycles (a) and dQ/dV dependence as a function of voltage for the third cycle (b) for the 9 wt.% and 20wt. % carbon-containing composites. (Si-content = 20 wt.%).

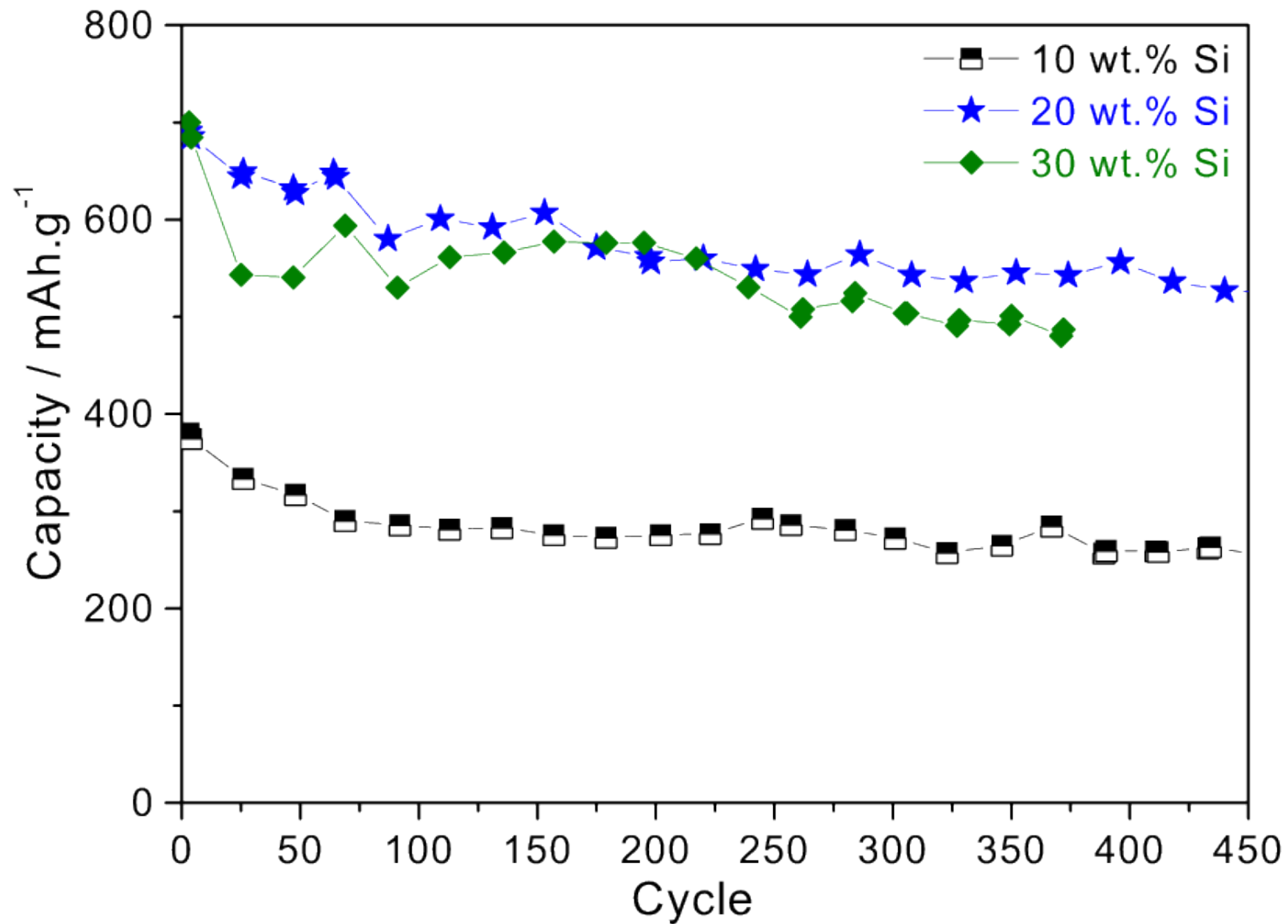


Fig. 8. Reversible capacity on cycling for the composites with constant C-amount (13wt.%) and increasing Si-content from 10 to 30 wt.%. Only reference cycles are shown. The first point corresponds to cycle 3 considered as the first reference cycle after two initial activation cycles.

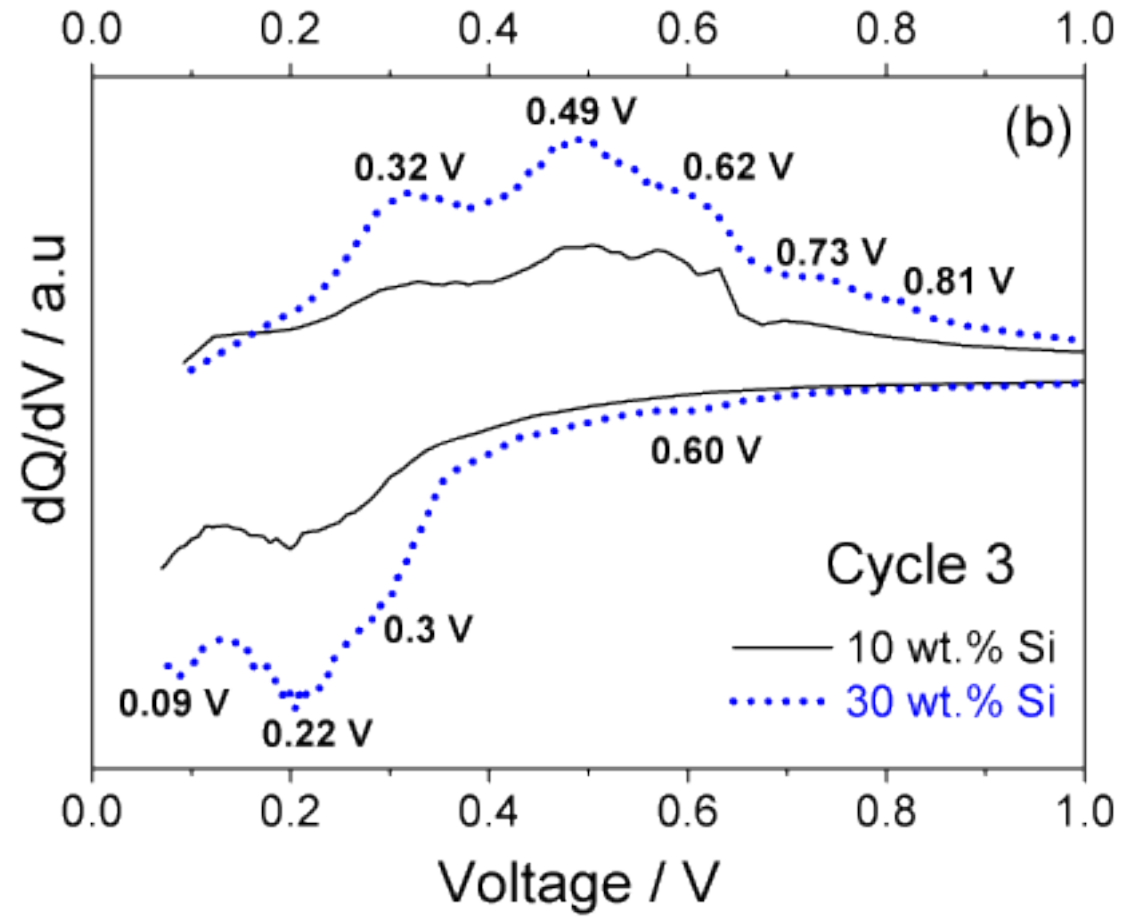
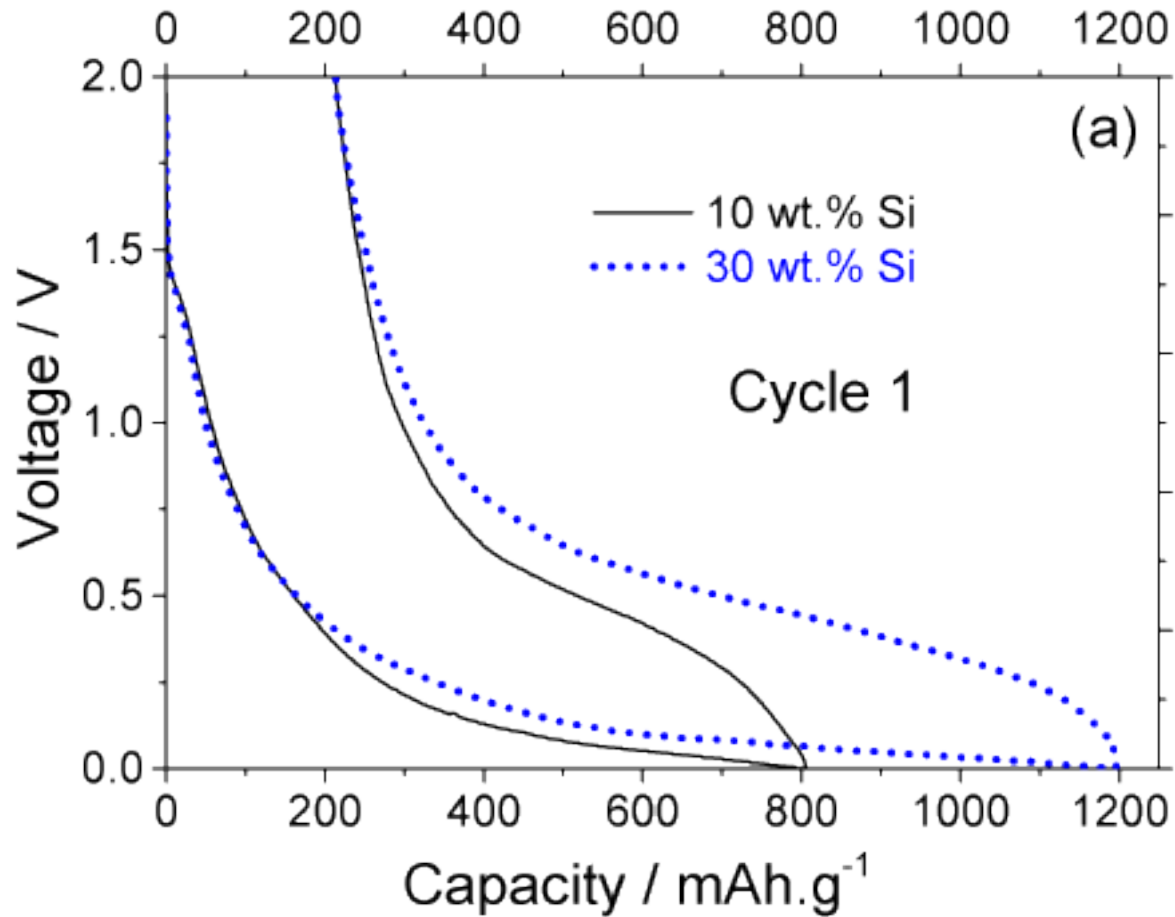


Fig. 9. Profiles of the first galvanostatic cycles (a) and dQ/dV dependence as a function of voltage for the third cycle (b) for the 10 wt.% and 30 wt.% silicon-containing composites (C-content = 13 wt.%).

Table 1. Composition (in wt.%) of Si-Ni-Sn-Al-C composites milled 20 hours with different carbon and silicon contents

	10 wt.% Si	20 wt.% Si	30 wt.% Si
0 wt.% C		$\text{Si}_{0,22}\text{Ni}_{0,22}\text{Sn}_{0,53}\text{Al}_{0,03}$	
9 wt.% C		$\text{Si}_{0,20}\text{Ni}_{0,20}\text{Sn}_{0,48}\text{Al}_{0,03}\text{C}_{0,09}$	
13 wt.% C	$\text{Si}_{0,10}\text{Ni}_{0,22}\text{Sn}_{0,52}\text{Al}_{0,03}\text{C}_{0,13}$	$\text{Si}_{0,19}\text{Ni}_{0,19}\text{Sn}_{0,46}\text{Al}_{0,03}\text{C}_{0,13}$	$\text{Si}_{0,30}\text{Ni}_{0,16}\text{Sn}_{0,38}\text{Al}_{0,03}\text{C}_{0,13}$
17 wt.% C		$\text{Si}_{0,18}\text{Ni}_{0,18}\text{Sn}_{0,44}\text{Al}_{0,03}\text{C}_{0,17}$	
20 wt.% C		$\text{Si}_{0,18}\text{Ni}_{0,18}\text{Sn}_{0,42}\text{Al}_{0,03}\text{C}_{0,20}$	

Table 1. Crystallographic data for nanostructured composites. Ni over-stoichiometry (x) in $\text{Ni}_{3+x}\text{Sn}_4$ and crystallite size (L) for all phases are given. Standard deviations referred to the last digit are given in parenthesis.

Composition C (wt%)	Si (wt%)	Phase	Content (wt.%)	S.G.	$a(\text{Å})$	Cell parameters $b(\text{Å})$	$c(\text{Å})$	β ($^\circ$)	x values $\text{Ni}_{3+x}\text{Sn}_4$	L (nm)
0	20	$\text{Ni}_{3+x}\text{Sn}_4$	9 (1)	$C2/m$	12.199*	4.0609*	5.2238*	105.17*	0.1*	10*
		Si	13 (1)	$Fd-3m$	5.430*					15 (2)
		Sn	43 (1)	$I4_1/amd$	5.8303 (2)		3.1822 (1)			27 (1)
		NiSi_2	35 (2)	$Fm-3m$	5.4731 (5)					5 (1)
9	20	$\text{Ni}_{3+x}\text{Sn}_4$	79(1)	$C2/m$	12.273 (1)	4.0421 (4)	5.2007 (5)	104.73 (1)	0.29 (3)	8 (1)
		Si	14 (1)	$Fd-3m$	5.430*					14 (2)
		Sn	3.2 (2)	$I4_1/amd$	5.830*		3.182*			22*
		NiSi_2	4 (1)	$Fm-3m$	5.470*					6*
13	20	$\text{Ni}_{3+x}\text{Sn}_4$	75 (1)	$C2/m$	12.299 (1)	4.0497 (3)	5.2043 (4)	104.67 (1)	0.29 (3)	8 (1)
		Si	17 (1)	$Fd-3m$	5.430*					14 (1)
		Sn	2.5 (4)	$I4_1/amd$	5.830*		3.182*			22*
		NiSi_2	5 (1)	$Fm-3m$	5.470*					6*
17	20	$\text{Ni}_{3+x}\text{Sn}_4$	74 (1)	$C2/m$	12.410 (1)	4.0685 (3)	5.2010 (6)	104.04 (1)	0.48 (3)	8 (1)
		Si	22 (1)	$Fd-3m$	5.430*					14 (1)
		Sn	0.9 (2)	$I4_1/amd$	5.830*		3.182*			22*
		NiSi_2	2 (1)	$Fm-3m$	5.470*					6*
20	20	$\text{Ni}_{3+x}\text{Sn}_4$	72 (1)	$C2/m$	12.452 (1)	4.0800 (1)	5.2089 (2)	103.60 (1)	0.60 (3)	50 (3)
		Si	27 (1)	$Fd-3m$	5.430*					17 (2)
		Sn	0.7 (2)	$I4_1/amd$	5.830*		3.182*			22*
		NiSi_2	0 (1)	$Fm-3m$	5.470*					6*
13	10	$\text{Ni}_{3+x}\text{Sn}_4$	90 (2)	$C2/m$	12.392 (2)	4.0679 (4)	5.1994 (6)	104.18 (1)	0.47 (3)	9 (1)
		Si	9 (1)	$Fd-3m$	5.430*					14 (3)
		Sn	0.5 (2)	$I4_1/amd$	5.830*		3.182*			22*
		NiSi_2	0 (1)	$Fm-3m$	5.470*					6*
13	30	$\text{Ni}_{3+x}\text{Sn}_4$	57 (2)	$C2/m$	12.287(2)	4.0466(6)	5.2079(8)	104.65(1)	0.37 (5)	7 (1)
		Si	31 (1)	$Fd-3m$	5.430*					11 (2)
		Sn	6 (0.3)	$I4_1/amd$	5.830*		3.182*			22*
		NiSi_2	6 (1)	$Fm-3m$	5.470*					6*

*Values were fixed to ensure refinement stability due to strong peak overlapping (Si and NiSi_2 phases) or low phase amount

Table 3. Electrochemical properties for the composites milled 20 hours with different carbon and silicon contents. $C_{\text{upper-limit}}$ stands for the maximum expected capacity, $C_{\text{lith,1st}}$ and $C_{\text{delith,1st}}$ are the lithiation and delithiation capacities at first cycle, $C_{\text{irrev,1st}}$ is the irreversible capacity at first cycle and $C_{\text{rev,3rd}}$ and $C_{\text{rev,1000th}}$ are the reversible capacities at cycles 3 and 1000.

C/Si (wt.%)	$C_{\text{upper-limit}}$ (mAh g ⁻¹)	$C_{\text{lith,1st}}$ (mAhg ⁻¹)	$C_{\text{lith,1st}} /$ $C_{\text{upper-limit}}$ (%)	$C_{\text{delith,1st}}$ (mAhg ⁻¹)	$C_{\text{irrev,1st}}$ (%)	$C_{\text{rev, 3rd}}$ (mAhg ⁻¹)	$C_{\text{rev, 1000th}}$ (mAhg ⁻¹)	Capacity fade (%/cycle)*
0/20	1348	949	70	716	25	510	213 ^a	0.28 ^a
9/20	1260	1196	95	985	18	707	542	0.024
13/20	1219	1191	98	1008	15	698	429	0.039
17/20	1178	1146	97	956	17	711	311	0.056
20/20	1170	923	79	702	24	522	136	0.073
13/10	955	794	83	572	28	388	256 ^b	0.077 ^b
13/30	1535	1186	77	966	17	700	487 ^c	0.082 ^c

*Fading values are calculated from cycle 3 to cycle 1000 except for *a*, *b* and *c* compositions for which last measured cycle was 206, 450 and 372, respectively.

Declaration of interests

The authors declare that they have no known competing financial interests or personal relationships that could have appeared to influence the work reported in this paper.

The authors declare the following financial interests/personal relationships which may be considered as potential competing interests:

Tahar Azib: Conceptualization, Methodology, Validation, Writing - Original Draft **Claire Thaury:** Investigation, Conceptualization, Writing - Original Draft **Cécile Fariaut-Georges:** Investigation, Validation **Thierry Hézèque:** Resources, Data Curation **Fermin Cuevas:** Conceptualization, Methodology, Project administration, Funding acquisition, Writing - Original Draft **Christian Jordy:** Conceptualization, Methodology, Funding acquisition, **Michel Latroche:** Conceptualization, Methodology, Project administration, Funding acquisition, Writing - Original Draft

SUPPLEMENTARY INFORMATIONS

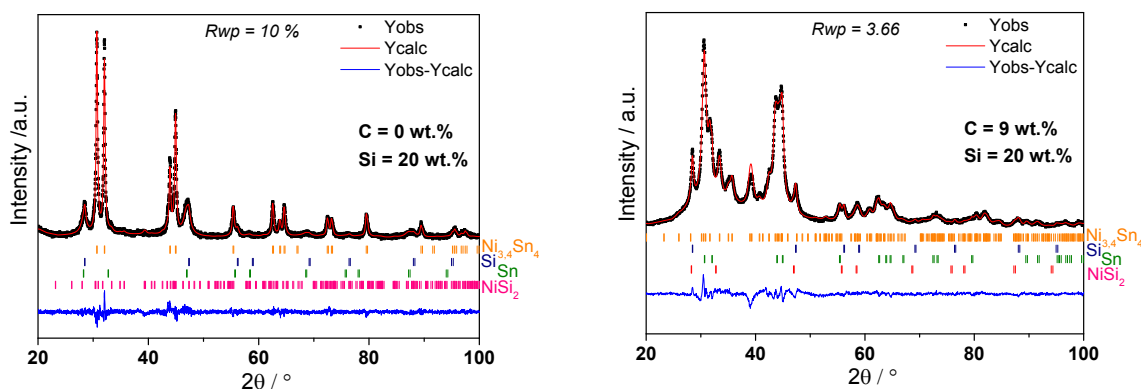
Role of silicon and carbon on the structural and electrochemical properties of Si-Ni_{3,4}Sn₄-Al-C anodes for Li-ion batteries

Tahar Azib^{a*}, Claire Thauray^{a,b*}, Cécile Fariaut-Georges^a, Thierry Hézèque^b, Fermin Cuevas^a, Christian Jordy^b and Michel Latroche^a

^aUniv. Paris Est Creteil, CNRS, ICMPE, UMR7182, F-94320, Thiais, France.

^bSAFT Batteries, 113 Bd. Alfred Daney, 33074 Bordeaux, France.

Figure S1 displays the graphical output of the Rietveld analysis of nanostructured composites Si-Ni_{3,4}Sn₄-Al-C with various carbon and silicon contents after 20-hour milling. All patterns can be indexed with main contribution of the two initials reactants (Si and Ni_{3,4}Sn₄), and minor contribution of two novel phases Sn and NiSi₂ produced during mechanical milling. Crystallographic data results of the Rietveld analysis are given in Table 2.



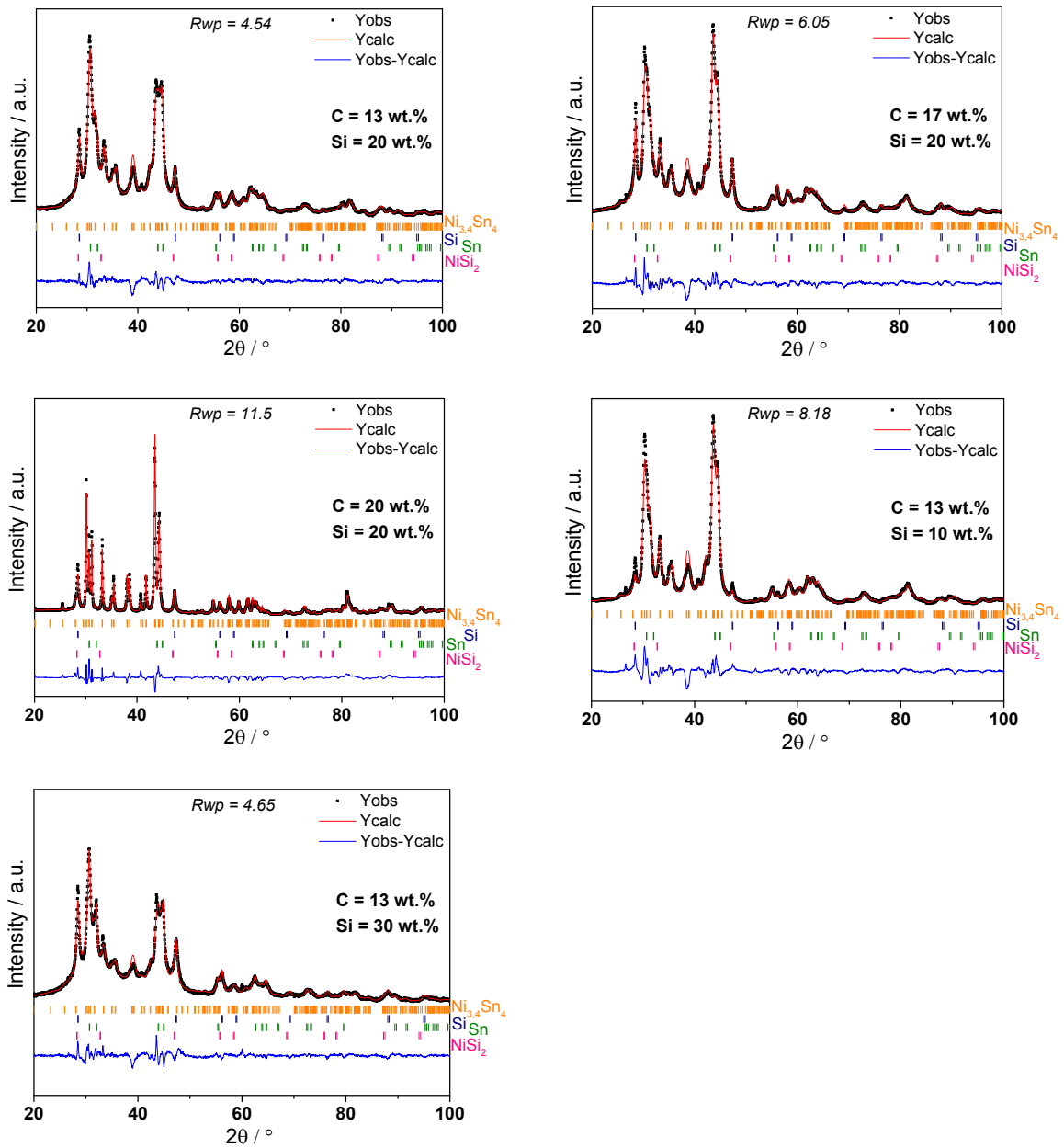


Fig. S1. Graphical output of Rietveld analysis for the seven composites studied in this work with various carbon and silicon contents.

Figure S2 displays the evolution of the lithiation/delithiation capacity on cycling for the carbon free composite. Rapid loss of capacity during the first cycles and poor cycling performance after 200 cycles (200 mAh/g) is observed.

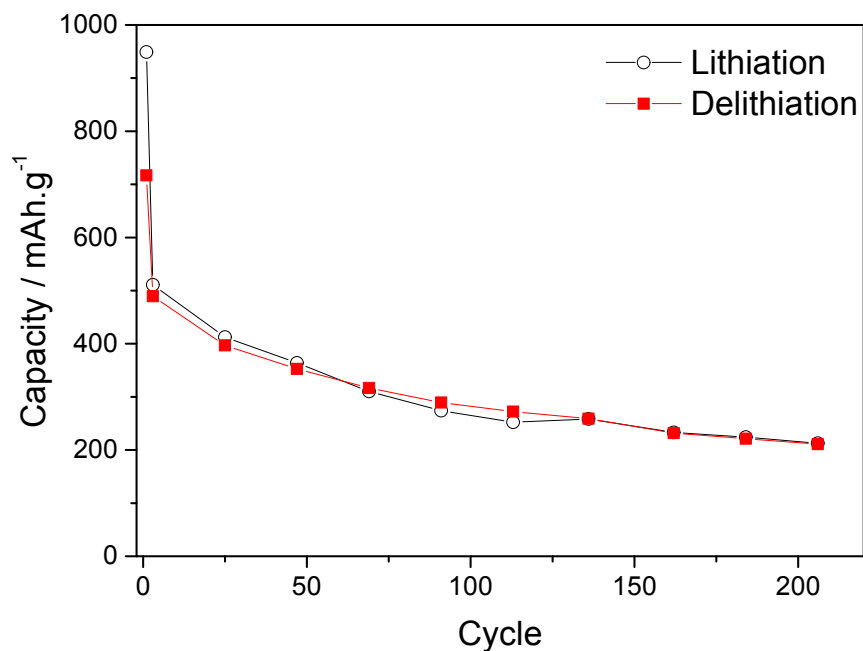


Fig. S2. Galvanostatic cycling for the carbon free composite. Only the first cycle and the reference ones are shown.

Figure 3 shows the coulombic efficiency for the four composites at constant Si-amount (20 wt.%) and different carbon content during 1000 cycles. The coulombic efficiency is high (~99%) and stable for all composites, though for 20 wt.% C some fluctuations are observed.

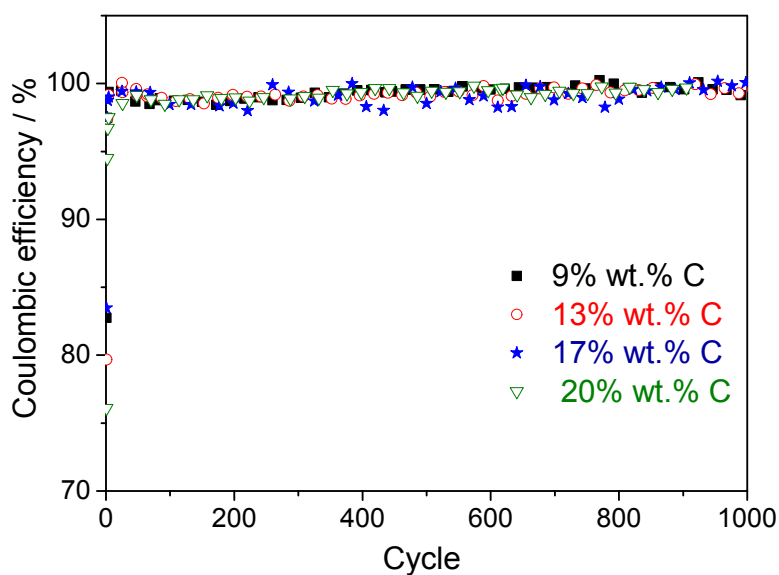


Fig. S3 Coulombic efficiency values for the four composites at constant Si-amount (20 wt.%) and increasing carbon content from 9 to 20 wt.%.

Figure 4 displays the coulombic efficiency for the four composites at constant C-amount (20 wt.%) and different silicon content during 450 cycles. The coulombic efficiency is high (~99%) and stable for all composites. Corresponding capacities are given in Figure 8.

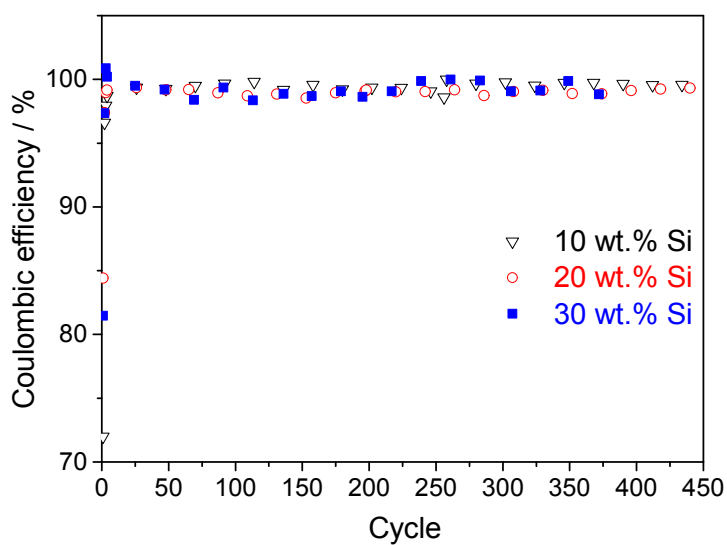


Fig. S4. Coulombic efficiency values for the 10 wt.% 20. wt% and 30 wt. % silicon-containing composites milled for 20 hours.